# CML

*Computer Mechanics Laboratory*

## *Technical Report No. 02-019*

# *THE EFFECTS OF E-BLOCK ARM THICKNESS ON THE AIRFLOW PAST THE HEAD STACK ASSEMBLY IN A MODELED HARD DISK DRIVE*


***Hany M. Gross, David B. Bogy, and Ömer Savas***

***Computer Mechanics Laboratory***

***Department of Mechanical Engineering***

***University of California, Berkeley 94720-1740***

***Toru Watanabe***

***HDD Division, Fujitsu Ltd.***

***4-4-1 Kamikodanaka, Nakahara-ku,***

***Kawasaki, 211-8588, Japan***



***December 2002***

## *Abstract*

*The effects of E-block arm thickness on the airflow past the head stack assembly in a modeled hard disk drive were investigated. The primary objective of this work was to shed some light on head vibration results that were presented in an earlier study. Four different E-block arm thicknesses were used, ranging from 1.0 mm to 1.6 mm in steps of 0.2 mm. An additional arm of thickness 1.0 mm without the arm cutouts was also tested. Airflow speed was measured along a line past the head stack assembly using a constant-temperature hot-wire anemometer, with and without the head gimbal assemblies attached, at the inner diameter, the middle diameter, and the outer diameter radial positions. The flow measurements were used to compute the mean flow speed, the root mean square flow fluctuation, and the turbulence intensity profiles along the measurement line. At the inner diameter position, a correlation was observed between the trend followed by the root mean square flow fluctuations in the region downstream of the E-block arm tip and that followed by vibration RMS component containing the structural resonances of the head stack assembly. The results reported in this study were found to be repeatable.*

## *Table of Contents*

***Section . . . . . page***

Abstract . . . . . ii

Table of Contents . . . . . .iii

List of Tables . . . . . iv

List of Figures . . . . . iv

1. Introduction . . . . . 1

2. Experimental Setup . . . . . 4

3. Experimental Results and Discussion . . . . . 6

3.1. E-block Case . . . . . .7

3.1.1. ID Position . . . . . .7

3.1.2. MD Position . . . . . .10

3.1.3. OD Position . . . . . .12

3.2. HSA Case . . . . . .13

3.2.1. ID Position . . . . . .13

3.2.2. MD Position . . . . . .15

3.2.3. OD Position . . . . . .15

4. Conclusion . . . . . .16

5. Acknowledgements . . . . . .18

6. References . . . . . .19

## *List of Tables*


Table 1 Blockage factors for the E-block arms at the ID, MD, and OD.

Table 2 Change in arm tip geometry due to attaching the HGA's; side view.


## *List of Figures*


Figure 1 Modeled hard disk drive.

Figure 2 A close-up of the HSA.

Figure 3 A close-up of the HGA.

Figure 4 Airflow measurement line, with the HGA’s attached, at the ID.

Figure 5 Measurement points.

Figure 6 Schematic of setup.

Figure 7 Schematic of hot-wire anemometer.

Figure 8 Radial distance of measurement points from disk center; ID, MD, and OD.

Figure 9 Mean flow speed profiles for unobstructed flow, t10, t12, t14, and t16; ID; “E-block arm”. Disk surface speed profile shown.

Figure 10 Mean unobstructed flow speed as a percentage of disk surface speed; ID; “E-block arm”.

Figure 11 Mean flow speed profiles for t10 and n10; ID; “E-block arm”.

Figure 12 RMS flow fluctuation profiles for unobstructed flow, t10, t12, t14, and t16; ID; “E-block arm”.

Figure 13 Turbulence intensity profiles for unobstructed flow, t10, t12, t14, and t16; ID; “E-block arm”.

Figure 14 RMS flow fluctuation profiles downstream of arm tip; ID; “E-block arm”.

Figure 15 Average normalized flow fluctuation vs. arm thickness; ID; “E-block arm”.

Figure 16 2-20 kHz RMS component amplitudes of head off-track vibration vs. arm thickness; ID.

Figure 17 RMS flow fluctuation profiles for t10 and n16; ID; “E-block arm”.

Figure 18 Turbulence intensity profiles for t10 and n16; ID; “E-block arm”.

Figure 19 Power spectra of flow fluctuation; unobstructed flow; ID; “E-block arm”.

Figure 20 Power spectra of flow fluctuation; t10; ID; “E-block arm”.

Figure 21 Power spectra of flow fluctuation; t12; ID; “E-block arm”.

Figure 22 Power spectra of flow fluctuation; t14; ID; “E-block arm”.

Figure 23 Power spectra of flow fluctuation; t16; ID; “E-block arm”.

Figure 24 Power spectra of flow fluctuation; n10; ID; “E-block arm”.

Figure 25 Mean flow speed profiles for unobstructed flow, t10, t12, t14, and t16; MD; “E-block arm”. Disk surface speed profile shown.

Figure 26 Mean unobstructed flow speed as a percentage of disk surface speed; MD; “E-block arm”.

Figure 27 Mean flow speed profiles for t10 and n10; MD; “E-block arm”.

Figure 28 RMS flow fluctuation profiles for unobstructed flow, t10, t12, t14, and t16; MD; “E-block arm”.

Figure 29 Turbulence intensity profiles for unobstructed flow, t10, t12, t14, and t16; MD; “E-block arm”.

Figure 30 RMS flow fluctuation profiles for t10 and n10; MD; “E-block arm”.

Figure 31 Turbulence intensity profiles for t10 and n10; MD; “E-block arm”.

Figure 32 Power spectra of flow fluctuation; unobstructed flow; MD; “E-block arm”.

Figure 33 Power spectra of flow fluctuation; t10; MD; “E-block arm”.

Figure 34 Power spectra of flow fluctuation; t12; MD; “E-block arm”.

Figure 35 Power spectra of flow fluctuation; t14; MD; “E-block arm”.

Figure 36 Power spectra of flow fluctuation; t16; MD; “E-block arm”.

Figure 37 Power spectra of flow fluctuation; n10; MD; “E-block arm”.

Figure 38 Mean flow speed profiles for unobstructed flow, t10, t12, t14, and t16; OD; “E-block arm”.

Figure 39 Mean flow speed profiles for t10 and n10; OD; “E-block arm”.

Figure 40 RMS flow fluctuation profiles for unobstructed flow, t10, t12, t14, and t16; OD; “E-block arm”.

Figure 41 Turbulence intensity profiles for unobstructed flow, t10, t12, t14, and t16; OD; “E-block arm”.

Figure 42 RMS flow fluctuation profiles for t10 and n10; OD; “E-block arm”.

Figure 43 Turbulence intensity profiles for t10 and n10; OD; “E-block arm”.

Figure 44 Power spectra of flow fluctuation; unobstructed flow; OD; “E-block arm”.

Figure 45 Power spectra of flow fluctuation; t10; OD; “E-block arm”.

Figure 46 Power spectra of flow fluctuation; t12; OD; “E-block arm”.

Figure 47 Power spectra of flow fluctuation; t14; OD; “E-block arm”.

Figure 48 Power spectra of flow fluctuation; t16; OD; “E-block arm”.

Figure 49 Power spectra of flow fluctuation; n10; OD; “E-block arm”.

Figure 50 Mean flow speed profiles for unobstructed flow, t10, t12, t14, and t16; ID; “HSA”. Disk speed profile shown.

Figure 51 Mean flow speed profiles for t10 and n10; ID; “HSA”.

Figure 52 RMS flow fluctuation profiles for unobstructed flow, t10, t12, t14, and t16; ID; “HSA”.

Figure 60 Power spectra of flow fluctuation; t16; ID; “HSA”.

Figure 61 Power spectra of flow fluctuation; n10; ID; “HSA”.

Figure 62 Mean flow speed profiles for unobstructed flow, t10, t12, t14, t16, and n10; MD; “HSA”. Disk surface speed profile shown.

Figure 63 RMS flow fluctuation profiles for unobstructed flow, t10, t12, t14, t16, and n10; MD; “HSA”.

Figure 64 Turbulence intensity profiles for unobstructed flow, t10, t12, t14, t16, and n10; MD; “HSA”.

Figure 65 Mean flow speed profiles for unobstructed flow, t10, t12, t14, t16, and n10; OD; “HSA”. Disk surface speed profile shown.

Figure 66 RMS flow fluctuation profiles for unobstructed flow, t10, t12, t14, t16, and n10; OD; “HSA”.

Figure 67 Turbulence intensity profiles for unobstructed flow, t10, t12, t14, t16, and n10; OD; “HSA”.

## *1. Introduction*

The hard disk drive (HDD) industry is continually faced with demands for higher areal recording densities, faster data transfer rates, and higher reliability. The demand for a higher areal recording density can be met by increasing the track density and/or the linear bit density. Track misregistration (TMR) and flying height modulation (FHM) must both be squeezed into tighter budgets in order to achieve such increases in the track and linear bit densities. On the other hand, the demand for higher data transfer rates has necessitated faster disk rotation speeds. Such high disk speeds lead to greater flow velocities, and, in turn, to higher levels of aerodynamic forces in the drive. The flow field generated in the drive excites the structural modes of the head stack assembly (HSA) and of the disks, inducing TMR and FHM. Consequently, it is of paramount importance to understand the nature and characteristics of the flow in HDD's if the performance of future drive generations is to be improved.

Early research on the effects of airflow in HDD's on suspension vibration was carried out by Yamaguchi *et al.* [1], whose results indicated that the amplitude of suspension vibration was proportional to the square of the approaching velocity. In their subsequent papers [2, 3], Yamaguchi *et al.* measured the flow around a suspension using hot-wire anemometry to identify the sources of suspension vibration, and carried out numerical simulations of the flow. They showed that suspension vibration was caused by the turbulence behind the suspension, and that applying an airfoil shape to the suspension cross-section can reduce its vibration.

The flow field between fully-shrouded co-rotating disks was numerically investigated by Iglesias *et al*, who concluded that there were significant vertical velocity fluctuations at the disk outer region, which resulted in disk flutter. The presence of the E-block arm between the disks in an actual HDD gives rise to a more complicated flow structure. The effects of a radially-inserted obstruction on the flow were studied in [5, 6, 7]. Abrahamson *et al*. [5] performed flow visualization experiments using a dye-injection technique on a modeled HDD, but did not consider the effects of the head gimbal assembly (HGA). Vortex shedding from the arm tip was observed. Harrison *et al*. [6] measured the flow field around an arm using hot-wire anemometry, and showed that the mean flow velocity increased as the disks were shrouded and/or as the disk spacing was decreased. Suzuki *et al*. [7] performed a numerical investigation of the flow around the arm, and showed that the insertion of the arm between co-rotating disks caused disk flutter and power losses due to windage.

Current HDD's employ in-line type HSA's, where the sliders are in-line with the suspension and E-block arms. Girard *et al.* [8] carried out flow visualization experiments for in-line type HSA's, and observed vortex shedding around the arm tip. However, they did not investigate the flow-induced vibration of the HSA, and its associated effects on TMR.

Gross et al. [9] investigated the effects of E-block arm thickness on head vibration in the off-track direction in a modeled HDD. Four different E-block arm thicknesses, ranging from 1.0 mm to 1.6 mm in steps of 0.2 mm, were tested at three radial positions:

the inner diameter (ID), the middle diameter (MD), and the outer diameter (OD). The RMS amplitudes of the off-track vibration were evaluated over the 0-20 kHz range, and were broken down into components over the 0-2 kHz and 2-20 kHz frequency bands in order to assess the contributions of the structural resonances to the overall head off-track vibration. The 2-20 kHz component was further divided into subcomponents over three frequency bands in order to evaluate the contributions of the E-block arm dynamics and the suspension dynamics to the overall vibration. The measured off-track RMS amplitudes were dependent on the E-block arm thickness. The RMS amplitudes, for all radial positions, increased as the arm thickness was increased. This trend was also observed in the 0-2 kHz component amplitudes. This trend, however, was not observed in the 2-20 kHz component amplitudes. The latter amplitudes increased as the arm thickness was increased to attain their highest values at the 1.2 mm arm thickness, and then decreased as the arm thickness was increased further to attain their lowest values at the 1.6 mm thickness. This trend in the observed off-track vibration was strongly shaped by the component of off-track resulting from the E-block arm dynamics.

In this study, the effects of E-block arm thickness on the airflow were investigated in the same modeled drive that was tested in [9]. The same E-block arms, of thicknesses 1.0 mm, 1.2 mm, 1.4 mm, and 1.6 mm, were used. Airflow measurements were taken along a line past the E-block arm and the HGA's using a constant-temperature hot-wire anemometer, with and without the HGA's attached, at three radial positions: the ID, the MD, and the OD. These flow measurements were conducted primarily with the objective of shedding some light on the head vibration results presented in [9], especially the

unexpected trend observed in the 2-20 kHz component. At the ID position, a correlation was observed between the trend followed by the RMS flow fluctuations in the region downstream of the E-block arms and that followed by the 2-20 kHz vibration RMS component amplitudes presented in [9].

## *2. Experimental Setup*

The same modeled drive that was used by Gross et al. [9] was used for this study. The setup, which is shown in Fig. 1, was described in detail in [9]. Photographs of the HSA and the HGA are presented in Figs. 2 and 3, respectively. The drive was operated at 10,000 rpm, the disk diameter was 84 mm, and the disk spacing 2.0 mm. The four E-block arms tested[1] had thicknesses of 1.0 mm, 1.2 mm, 1.4 mm and 1.6 mm. These arms will henceforth be referred to as t10, t12, t14 and t16, respectively. An additional arm of thickness 1.0 mm without the arm cutouts was also tested. This arm will henceforth be referred to as n10. The arm tip thickness at the swage area was 0.95 mm for all arms. In the HGA, the baseplate thickness was 0.2 mm; the loadbeam thickness was 0.038 mm at the bend area and beyond the dimple, and 0.68 mm between the bend area and the dimple; and the slider thickness was 0.305 mm.

The flow speed was measured with and without HGA's attached to the arms, at the ID, the MD, and the OD. Airflow measurements were taken along a line parallel to

[1] The E-block arms are the same ones used in [9].

the E-block arm trailing edge, at a distance of 4 mm from the edge. Figure 4 is a drawing to scale that shows the exact position of the measurement line (with the HGA's attached, and the slider at the ID). The airflow speed was measured at 30 points along this line, with a step size of 1.27 mm (0.05 in) from one point to the next. The measurement points along with the disk edge positions at the ID, MD, and OD are depicted in Fig. 5, which is also to scale. The position of these points was not changed throughout this study. Figure 6 is a schematic of the setup that highlights several critical dimensions.

A customized constant-temperature hot-wire anemometer (TSI model 1276CF-10A) was used for measuring the flow field. Figure 7 shows a schematic of the hot-wire probe used. The body length of the anemometer probe was extended, so that it could be inserted between the two disks. The probe diameter was 0.9 mm, the sensor diameter 4 μm, and the sensor length 0.2 mm, which is 10% of the disk separation. The sensor was oriented with its axis parallel to the spin axis of the disks, and was centered between the two disks. Therefore, the sensor was most sensitive to the in-plane flow velocity component at the mid-plane between the disks. The output of the hot-wire anemometer was fed to an HP3562A signal analyzer. At each measurement point, the hot-wire anemometer output was averaged in the time domain to obtain the mean flow speed, $\hat{u}$. The dc component of the anemometer output was then removed, and the output was averaged in the frequency domain to obtain an averaged power spectrum of the flow fluctuation, $\overline{(u'(f))^2}$, where $u'$ is the flow fluctuation, and $f$ is frequency. The fluctuation power spectra were used to estimate the RMS flow fluctuation, $u_{rms}$, according to

$$u_{rms} = \sqrt{h \sum_i \overline{(u'(f_i))^2}} \,, \qquad (1)$$

where $h$ is a scale factor for the windowing function. A Hanning window was used in these measurements. The scale factor $h$ is 2/3 for a Hanning window in the HP3563A.

The RMS flow fluctuation is usually expressed as a percentage of the mean flow speed. This percentage is known as the turbulence intensity, $TI$, of the flow, and it was computed at each measurement point according to

$$TI = \frac{u_{rms}}{\bar{u}} \,. \qquad (2)$$

The disk surface speed $V_d$ was computed according to

$$V_d = \omega r \,, \qquad (3)$$

where $\omega$ is the disk angular speed ($\omega$ = 1,047.2 rad/s at a disk rotational speed of 10,000 rpm).

## *3. Experimental Results and Discussion*

The mean flow speed and RMS flow fluctuation were measured and evaluated along the measurement line for each of the five E-block arms, as well as for the unobstructed flow (where no arm were inserted between the disks), at the ID, MD, and OD. Two sets of measurements were taken: the first with no HGA's attached to the arms (“E-block arm” case), and the second with the HGA's attached (“HSA” case). The

blockage factors associated with each of the E-block arms at the ID, MD, and OD positions are listed in Table 1. The radial distance $R$ of the measurement points from the disk center is plotted in Fig. 8 for the ID, MD, and OD positions. It should be noted that point 29 is the last measurement point between the disks at the ID position, point 24 is the last measurement point between the disks at the MD position, and the measurement line is completely outside the disks at the OD position.

## *3.1. Case I: E-block arm*

### *3.1.1. ID Position*

The results presented in this section are for the "E-block arm" case at the ID position. Figures 9(a) and 9(b) show the mean flow speed profiles along the measurement line for t10, t12, t14, and t16. The unobstructed flow speed and disk surface speed profiles along the measurement line are also plotted for reference in Fig. 9(a). In Fig. 9(b), the unobstructed flow speed and the disk speed profiles were removed to allow for a better comparison of the E-block arms. It should be noted that the disk surface speed profile is not a straight line because the measurement line is not a radial line on the disk.

Figure 9(a) indicates that the unobstructed flow speed increased as the disk surface speed increased, up until index 23, which is 7.62 mm (0.3 in) away from the disk edge. Figure 10 is a plot of the mean unobstructed flow speed as a percentage of the disk surface speed, and it shows that up until around 2 mm away from the disk edge (position index 27), the mean flow speed of the unobstructed flow along the measurement line at the ID was in the range of 64%-87% of the disk surface speed.

A comparison of the unobstructed and the obstructed flow speed profiles in Fig. 9(a) illustrates that inserting the arms between the disks resulted in a drop in the flow speed past the arms, and an increase in the flow speed in the region near the hub. This is an expected result since inserting an arm between the disks partially blocks the flow and redirects it towards the hub along the arm leading edge, as observed in the flow visualizations carried out by Girard et al [8]. Figure 9(b) shows that as the arm thickness was increased, a higher drop in the flow speed past the arm and a greater increase in the flow speed near the hub resulted, as more of the flow was blocked at the arm and redirected towards the hub. Figure 11 is a plot of the mean flow speed profiles along the measurement line for t10 and n10. These profiles indicate that the presence of the arm cutout holes and the bridge between them resulted in the trough observed around indices 23 and 24, and in blocking more of the flow at the arm and redirecting more flow towards the hub. The troughs observed for the other arms in Fig. 9 between indices 23 and 27 are also expected to be the result of the arm cutout holes and the bridge between them.

Figure 12 shows the RMS flow fluctuation profiles along the measurement line for the unobstructed flow, t10, t12, t14, and t16. These profiles show that inserting an arm between the disks substantially increased the flow fluctuation level between the disks. They also show that the region near the disk edge exhibited high flow fluctuation levels, even in the unobstructed flow case. This high fluctuation region was likely to be the result of the air inflow and outflow at the shroud cutout. Figure 13 depicts the turbulence intensity profiles for the unobstructed flow, t10, t12, t14, and t16. These profiles show

that significant levels of turbulence were generated due to the presence of the arms between the disks.

An interesting feature in Fig. 12 is the trend that the RMS flow fluctuation in the region downstream of the E-block arm tip followed as the arm thickness was changed. A close up of this region of the measurement line is presented in Fig. 14(a). The figure shows that the flow fluctuation level in this region increased as the arm thickness was increased from 1.0 mm to 1.2 mm, then decreased as the arm thickness was increased from 1.2 mm to 1.4 mm, and then decreased further as the arm thickness was increased from 1.4 mm to 1.6 mm. In order to capture this trend more clearly, the profiles of Fig. 14(a) were normalized by the profile of t12. The normalized profiles are depicted in Fig. 14(b). The average of each normalized profile was calculated, and was plotted in Fig. 15 against the corresponding arm thickness. The trend observed in this plot is very similar to the trend followed by the 2-20 kHz RMS component amplitudes of vibration as a function of arm thickness [9]. This trend is repeated in Fig. 16 for convenience. The similarity between Figs. 15 and 16 expresses a significant correlation between the RMS flow fluctuation in the region downstream of the E-block arm tip and the 2-20 kHz RMS component amplitudes of vibration. The observed correlation begs the investigation of the flow characteristics in the region immediately downstream of the arm tip. This is the subject of ongoing research. The results presented in this section were found to be repeatable. Figures 17 and 18 compare the RMS flow fluctuation and turbulence intensity profiles, respectively, of t10 and n10.

The power spectra of the flow fluctuations for the unobstructed flow at the measurement line in the ID position are plotted in Fig. 19. The figure contains 30 curves, which are the power spectra at the 30 measurement points. The peak observed in the spectra at 167 Hz corresponds to the disk rotation speed, and is due to disk runout. Most of the other peaks in these spectra are harmonics of the 167 Hz peak. Figures 20 through 24 show the power spectra for t10, t12, t14, t16, and n10. Two common features of all of these plots is that the disk runout peaks at 167 Hz are at lower amplitudes than they were in the unobstructed flow power spectra, and that the energy contained in the power spectra at frequencies higher than around 700 Hz was greater with any of the arms inserted between the disks than that of the unobstructed flow. No vortex shedding peaks were observed in any of the power spectra.

### *3.1.2. MD Position*

The results presented in this section are for the "E-block arm" case at the MD position. Figure 25 shows the mean flow speed profiles along the measurement line for t10, t12, t14, and t16. The unobstructed flow speed and disk surface speed profiles along the measurement line are also plotted for reference. Note that point 24 is the last measurement point between the disks. Figure 26 shows that up until around 2 mm away from the disk edge (position index 21), the mean flow speed of the unobstructed flow along the measurement line at the MD is in the range of 70%-87% of the disk surface speed.

A comparison of the unobstructed and obstructed flow speed profiles in Fig. 25 demonstrates that inserting the arms between the disks resulted in a drop in the flow speed past the arms. Although the measurement line at the MD position did not cover the region near the hub, an increase in the flow speed in that region is expected. Figure 25 illustrates that as the arm thickness was increased, a higher drop in the flow speed past the arm resulted, as more of the flow was blocked by the arm. Figure 27 is a plot of the mean flow speed profiles along the measurement line for t10 and n10. These profiles indicate that the presence of the arm cutout holes and the bridge between them resulted in lower flow speed past the arm, indicating that more flow was blocked by the arm.

Figures 28 and 29 depict the RMS flow fluctuation profiles and the turbulence intensity profiles along the measurement line for the unobstructed flow, t10, t12, t14, and t16. Although the RMS flow fluctuation profiles of the arms are around the same level as that of the unobstructed flow, the corresponding low mean velocity profiles of the arms yield a higher level of turbulence intensity, as shown in Fig. 29. Figure 29 also shows that increasing the arm thickness from 1.0 mm to 1.2 mm, and from 1.2 mm to 1.4 mm, resulted in higher turbulence intensity profiles. The turbulence intensity profiles for t14 and t16 were quite close.

Figures 30 and 31 compare the RMS flow fluctuation and turbulence intensity profiles, respectively, for t10 and n10. The lower levels of flow fluctuation observed for t10 in Fig. 30 are related to its accompanying lower mean flow speed profile (Fig. 27).

Figure 31 shows that the presence of the arm cutouts did not considerably affect the turbulence intensity level along the measurement line.

The power spectra of the flow fluctuation for the unobstructed flow and the different arms are presented in Figs. 32 through 37. The disk runout peak at 167 Hz was higher for t10 than it was for the unobstructed flow. For t12, the amplitude of this peak decreased to roughly the same level as it was for the unobstructed flow. The amplitude of the peak decreased further for t14, and even further for t16. The energy contained in the power spectra at frequencies higher than around 1 kHz was greater with any of the arms inserted between the disks than that of the unobstructed flow. No vortex shedding frequencies were observed in any of the MD power spectra.

### *3.1.3. OD Position*

The results presented in this section are for the "E-block arm" case at the OD position. The measurement line in this position was completely outside the two disks, and probably hardly captured any of the flow crossing the E-block arm tip. It is more likely to have measured the flow entering and leaving the space between the disks. Figure 38 shows the mean flow speed profiles along the measurement line for the unobstructed flow, t10, t12, t14, and t16. An examination of the unobstructed flow speed profiles reveals that the airflow was faster as the sensor approached the disk on the measurement line, attaining a peak at position index 10. Inserting the arms between the disks resulted in a drop in the flow speed past the arms. Figure 38 illustrates that as the arm thickness was increased, a higher drop in the flow speed past the arm resulted, as more of the flow

was blocked. Figure 39 is a plot of the mean flow speed profiles along the measurement line for t10 and n10. These profiles suggest that the presence of the arm cutout holes and the bridge between them resulted in blocking slightly more of the flow at the arm.

Figures 40 and 41 depict the RMS flow fluctuation profiles and the turbulence intensity profiles along the measurement line for the unobstructed flow, t10, t12, t14, and t16. Figure 41 shows that inserting the arms between the disks increased the turbulence intensity near the disk (indices 0-15). Figures 42 and 43 compare the RMS flow fluctuation and turbulence intensity profiles, respectively, for t10 and n10. The figures indicate that the flow was slightly more turbulent due to the presence of the arm cutouts.

The power spectra of the flow fluctuation for the unobstructed flow and the different arms are presented in Figs. 44 through 49. It should be noted that the disk runout peak at 167 Hz appeared in these spectra, but it did not stand out as it did in the ID and MD measurements. The energy contained in the power spectra of the flow fluctuation was higher with any of the arms inserted between the disks than it was for the unobstructed flow. No clear vortex shedding frequencies were observed in any of the OD power spectra.

## *3.2. Case II: HSA*

### *3.2.1. ID Position*

The results presented in this section are for the "HSA" case at the ID position. Figure 50 shows the mean flow speed profiles along the measurement line for the

unobstructed flow, t10, t12, t14, and t16. The disk surface speed profile along the measurement line is also plotted for reference. The mean flow speed profiles for the different arms were quite similar in character to the corresponding profiles in the "E-block arm" case (Fig. 9), and exhibited a significantly different behavior only in the range of position indices 10-15. The flow received by this portion of the measurement line was probably the flow crossing the swage area of the HSA, whose thickness and geometry were significantly modified by attaching the HGA's. The thickness of the arm at this region was increased from 0.95 mm to 1.35 mm as a result of the added thickness of the HGA baseplates, and its geometry was modified as shown in Table 2.

Figure 51 is a plot of the mean flow speed profiles along the measurement line for t10 and n10. The arm cutout holes and the bridge between them resulted in the trough observed around measurement point 23, and in blocking more of the flow at the arm and redirecting more flow towards the hub.

Figures 52 and 53 depict the RMS flow fluctuation and turbulence intensity profiles, respectively, along the measurement line for the unobstructed flow, t10, t12, t14, and t16. These profiles are very similar in character to the corresponding profiles in the "E-block arm" case (Figs. 12 and 13). The flow fluctuation profiles around the region past the arm tip followed the same trend as they did in the "E-block arm" case. Figure 54 presents the averages of the normalized profiles[2]. The trend observed in this plot is quite similar to those presented in Figs. 15 and 16, reinforcing the correlation between the

[2] These profiles were normalized by the t12 profile as was done in §3.1.1.

RMS flow fluctuation in the region downstream of the E-block arm tip and the 2-20 kHz RMS component amplitudes of vibration.

Figures 55 and 56 compare the RMS flow fluctuation and turbulence intensity profiles, respectively, for t10 and n10. These profiles exhibited the same behavior as that reported in §3.1.1 for the "E-block arm" case.

The power spectra of the flow fluctuations for t10, t12, t14, t16, and n10 are plotted in Figs. 57 through 61. As was the case in the "E-block arm" case, the power spectra exhibited the disk runout peaks at 167 Hz, which were at lower amplitudes than they were in the unobstructed flow power spectra; the energy contained in the power spectra at frequencies greater than around 700 Hz was greater with any of the arms inserted between the disks than that of the unobstructed flow; and no vortex shedding peaks were observed in any of the power spectra.

### *3.2.2. MD Position*

The results at the MD position for the "HSA" case are similar to those for the "E-block arm" case. Figures 62, 63, and 64 show the mean flow speed, the RMS flow fluctuation, and the turbulence intensity profiles, respectively, along the measurement line for the unobstructed flow, t10, t12, t14, t16, and n10. There were no significant differences between the power spectra of the "HSA" and "E-block arm" cases[3].

[3] The power spectra for the "HSA" case at the MD and OD positions are not presented in this report since they are not discernibly different from those of the "E-block arm" case.

### *3.2.3. OD Position*

The results presented in this section are for the "HSA" case at the OD position. Figures 65, 66, and 67 show the mean flow speed, the RMS flow fluctuation, and the turbulence intensity profiles, respectively, along the measurement line for the unobstructed flow, t10, t12, t14, t16, and n10. These profiles are qualitatively similar to the one obtained for the "E-block arm" case at the OD. With the exception of t16, all the arms exhibited higher mean flow speed profiles and lower RMS flow fluctuation profiles than the corresponding profiles obtained in the "E-block arm" case at the OD along most of the measurement line, which subsequently led to lower turbulence intensity profiles in the "HSA" case. There were no significant differences between the power spectra of the "HSA" and "E-block arm" cases[3].

## *4. Conclusion*

In this study, the effects of E-block arm thickness and the E-block arm cutouts on the airflow in a modeled disk drive were investigated experimentally. Four E-block arms (with arm cutouts) of thicknesses 1.0 mm, 1.2 mm, 1.4 mm, and 1.6 mm were used. An additional arm of thickness 1.0 mm with no arm cutouts was also tested. Airflow was measured, using a hot-wire anemometer, along a line past the HSA at the ID, the MD, and the OD positions, with and without the HGA's attached. The mean flow speed, RMS flow fluctuation, and turbulence intensity profiles along the measurement line were obtained for all arms. The results reported in this study were found to be repeatable.

The HGA's did not have a significant effect on the flow at the measurement line. For all radial positions, inserting an arm (with or without HGA's attached) between the disks resulted in a drop in the mean flow speed past the arm, indicating that the flow was partially blocked by the arm. In the ID case, an increase in the mean flow speed near the hub was observed, suggesting that the blocked flow was redirected towards the hub. As the arm thickness was increased, a higher drop in the mean flow speed past the arm resulted, and, in the ID position, a higher increase in the flow speed near the hub was observed. At all radial positions, the presence of the arm cutout holes and the bridge between them resulted in blocking more of the flow at the arm and redirecting more flow towards the hub.

Inserting the arms between the disks substantially increased the flow fluctuation and turbulence intensity levels along the measurement line at the ID position, increased the level of turbulence intensity along the measurement line at MD position, and increased the turbulence intensity at the segment of the line near the disk at the OD position. At the ID position, for both the “E-block arm” and the “HSA” cases, a significant correlation was observed between the RMS flow fluctuation in the region downstream of the E-block arm tip and the 2-20 kHz RMS component amplitudes of vibration. This correlation was repeatable and consistent. No such correlation could be observed at the MD and OD positions, since the measurement line at these positions was expected to receive very little of the flow crossing the arm tip.

A peak was observed at 167 Hz in all the flow fluctuation power spectra. It corresponded to the disk rotation speed, and was due to disk runout. No coherent vortex shedding peaks were observed in any of the power spectra. At the ID and MD positions, the energy contained in the power spectra at frequencies higher than around 700 Hz for the ID and 1 kHz for the MD was greater with any of the arms inserted between the disks than that of the unobstructed flow. At the OD position, the energy contained in the power spectra of the flow fluctuation was higher with any of the arms inserted between the disks than it was for the unobstructed flow.

## *5. Acknowledgements*

This study was supported by the Computer Mechanics Laboratory at the University of California at Berkeley, the Hard Disk Drive Division at Fujitsu Ltd., and the Information Storage Industry Consortium.

## *6. References*


[1] Yamaguchi, Y., Takahashi, K., Fujita, H. and Kuwahara, K., "Flow Induced Vibration of Magnetic Head Suspension in Hard Disk Drive", IEEE Transaction of Magnetics, Vol. 22, No. 5, September 1986, pp. 1022-1024.

[2] Yamaguchi, Y., Talukder, A. A., Shibuya, T. and Tokuyama, M., "Air Flow Around a Magnetic-Head-Slider Suspension and Its Effect on Slider Flying-Height Fluctuation", IEEE Transaction of Magnetics, Vol. 26, No. 5, September 1990, pp. 2430-2432.

[3] Tokuyama, M., Yamaguchi, Y., Miyata, S. and Kato, C., "Numerical Analysis of Flying-Height Fluctuation and Positioning Error of Magnetic Head due to Flow Induced by Disk Rotation", IEEE Transaction of Magnetics, Vol. 27, No. 6, November 1991, pp. 5139-5141.

[4] Iglesias, I. and Humphrey, J., "Two- and Three-Dimensional Laminar Flows Between Disks Co-Rotating in a Fixed Cylindrical Enclosure", International Journal for Numerical Methods in Fluids, Vol. 26, 1998, pp. 581-603.

[5] Abrahamson, S., Chiang, C. and Eaton, J. K., "Flow Structure in Head-Disk Assemblies and Implications for Design", Adv. Info. Storage Syst., Vol. 1, 1991, pp. 111-132.

[6] Harrison, J. C., Lou, D.H. and Talke, F. E., “AirFlow at the Tip of an Obstruction Between Corotaing Disks”, Advanced Information Storage Systems, Vol. 5, 1993, pp. 159-174.

[7] Suzuki, H. and Humphrey, J., “Flow Past Large Obstructions Between Corotating Disks in Fixed Cylindrical Enclosures”, ASME Journal of Fluids Engineering, Vol. 119, September 1997, pp. 499-505.

[8] Girard, J., Abrahamson, S. and Uznanski, K., “The Effect of Rotary Arms on Corotating Disk Flow”, ASME Journal of Fluids Engineering, Vol. 117, June 1995, pp. 259-262.

[9] Gross, H. M., Watanabe, T., and Bogy, D. B., “The Effects of E-Block Arm Thickness on Head Vibration Between Co-Rotating Disks in a Modeled Hard Disk Drive”, CML Technical Report, No. 02-013, December 2002.

| Arm | Thickness [mm] | Blockage Factor at ID | Blockage Factor at MD | Blockage Factor at OD |
|---|---|---|---|---|
| n10 | 1.0 | 27% | 22% | 15% |
| t10 | 1.0 | 27% | 22% | 15% |
| t12 | 1.2 | 31% | 26% | 18% |
| t14 | 1.4 | 36% | 30% | 21% |
| t16 | 1.6 | 40% | 34% | 24% |

Table 1: Blockage factors for the E-block arms at the ID, MD, and OD.

| Arm | Before inserting HGA's | After inserting HGA's |
|---|---|---|
| n10 | | 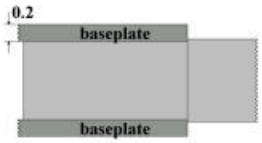 |
| t10 | | |
| t12 | | |
| t14 | | |
| t16 | 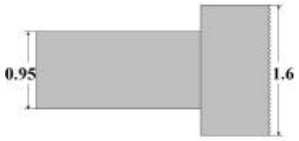 | |

Table 2: Change in arm tip geometry due to attaching the HGA's; side view. Dimensions in mm.

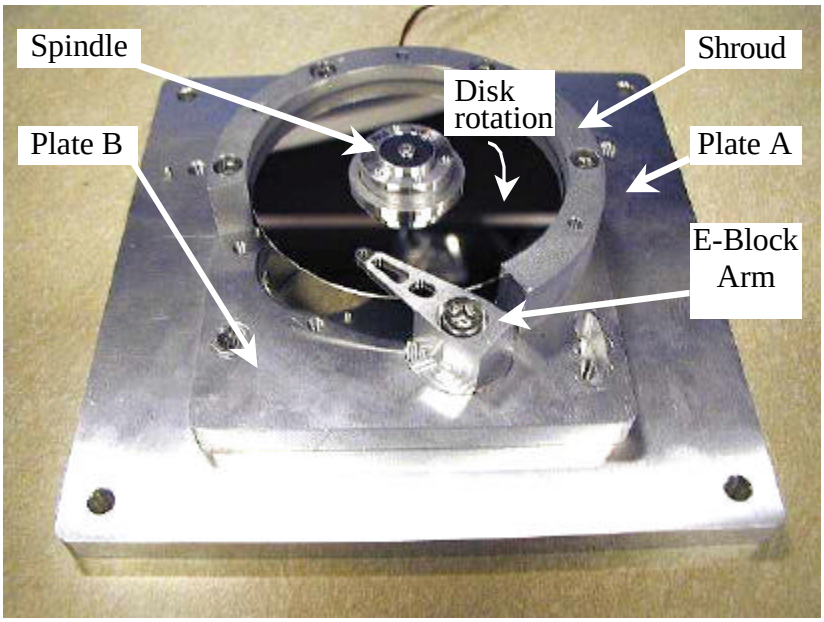


(a) Setup without top disk and cover

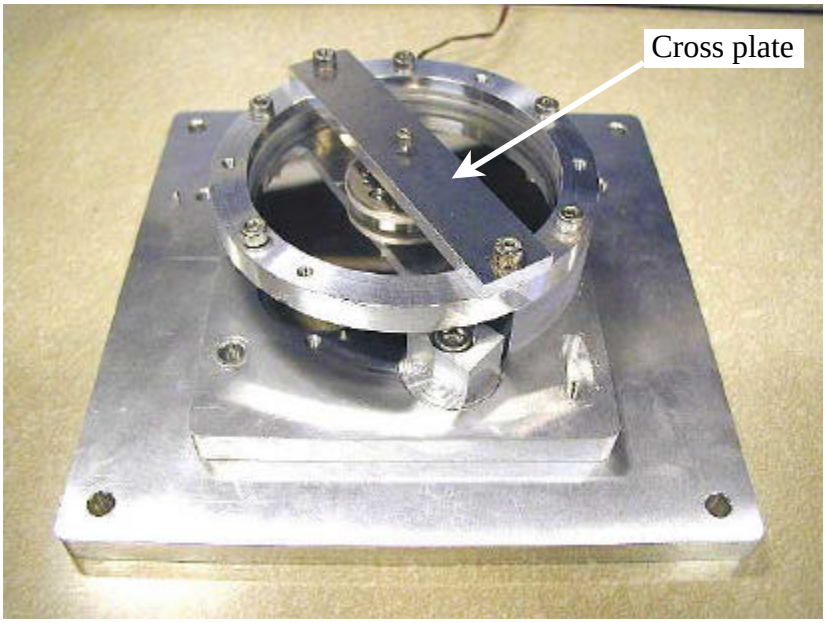


(b) Setup with top disk and cover
Figure 1: Modeled hard disk drive.

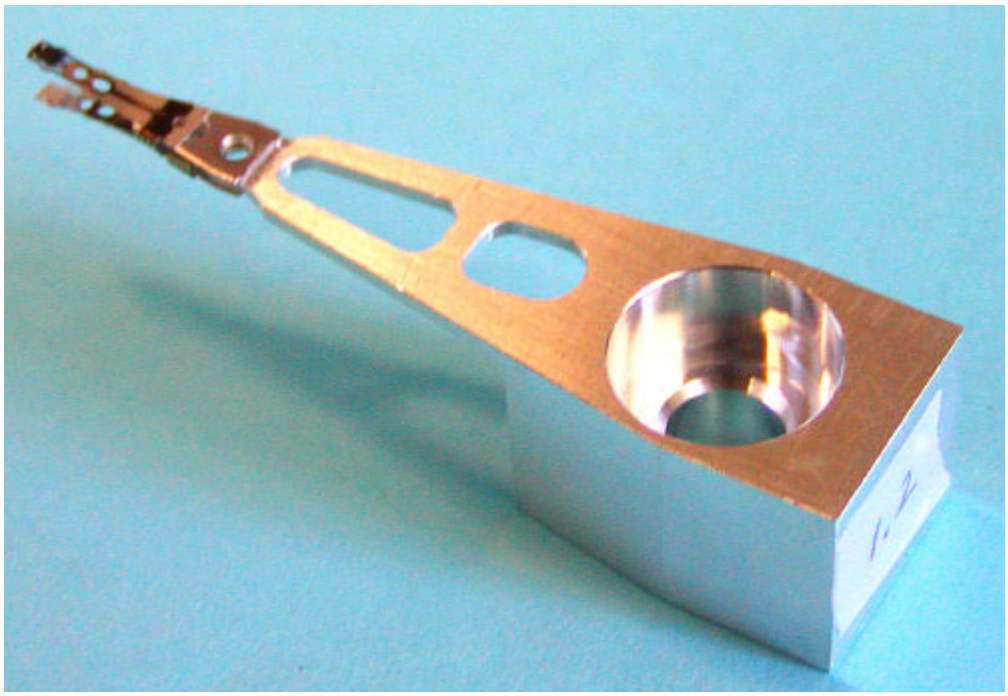

Figure 2: A close-up of the HSA.

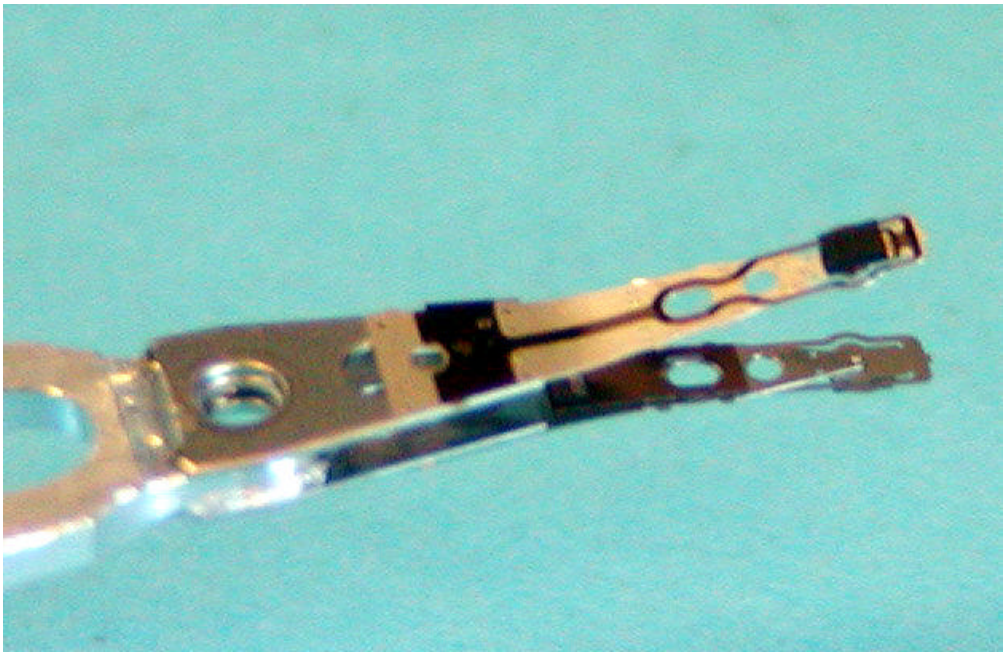

Figure 3: A close-up of the HGA.

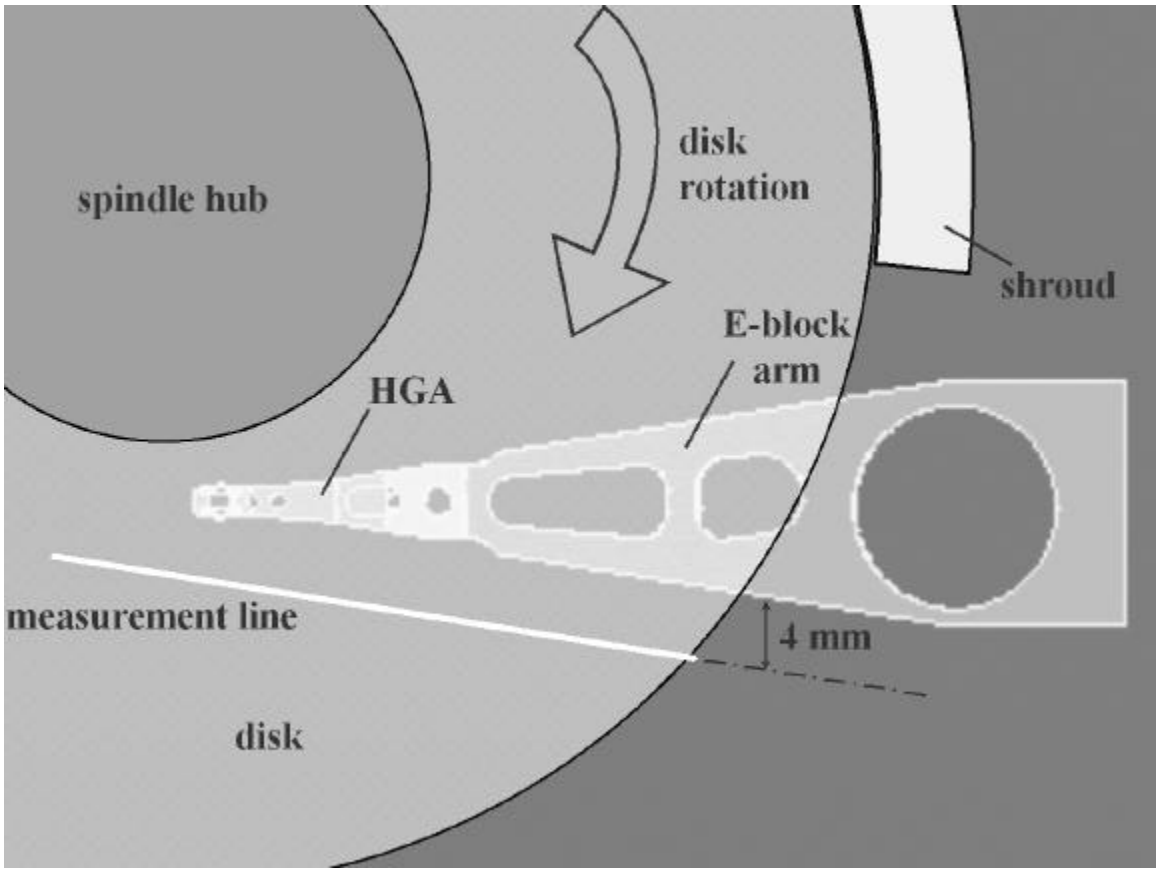


Figure 4: Airflow measurement line, with the HGA's attached, at the ID.

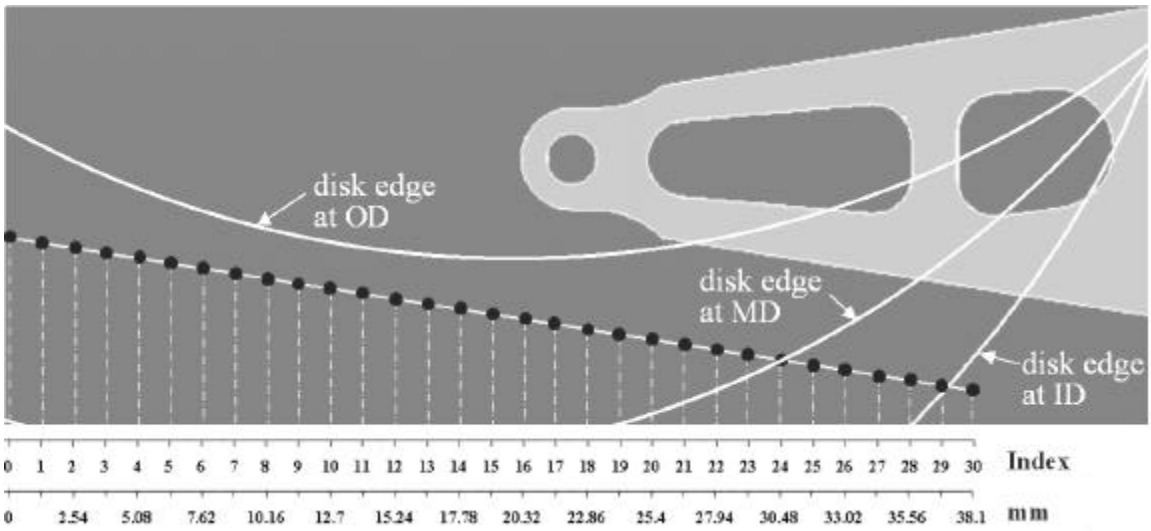


Figure 5: Measurement points, marked by (●).

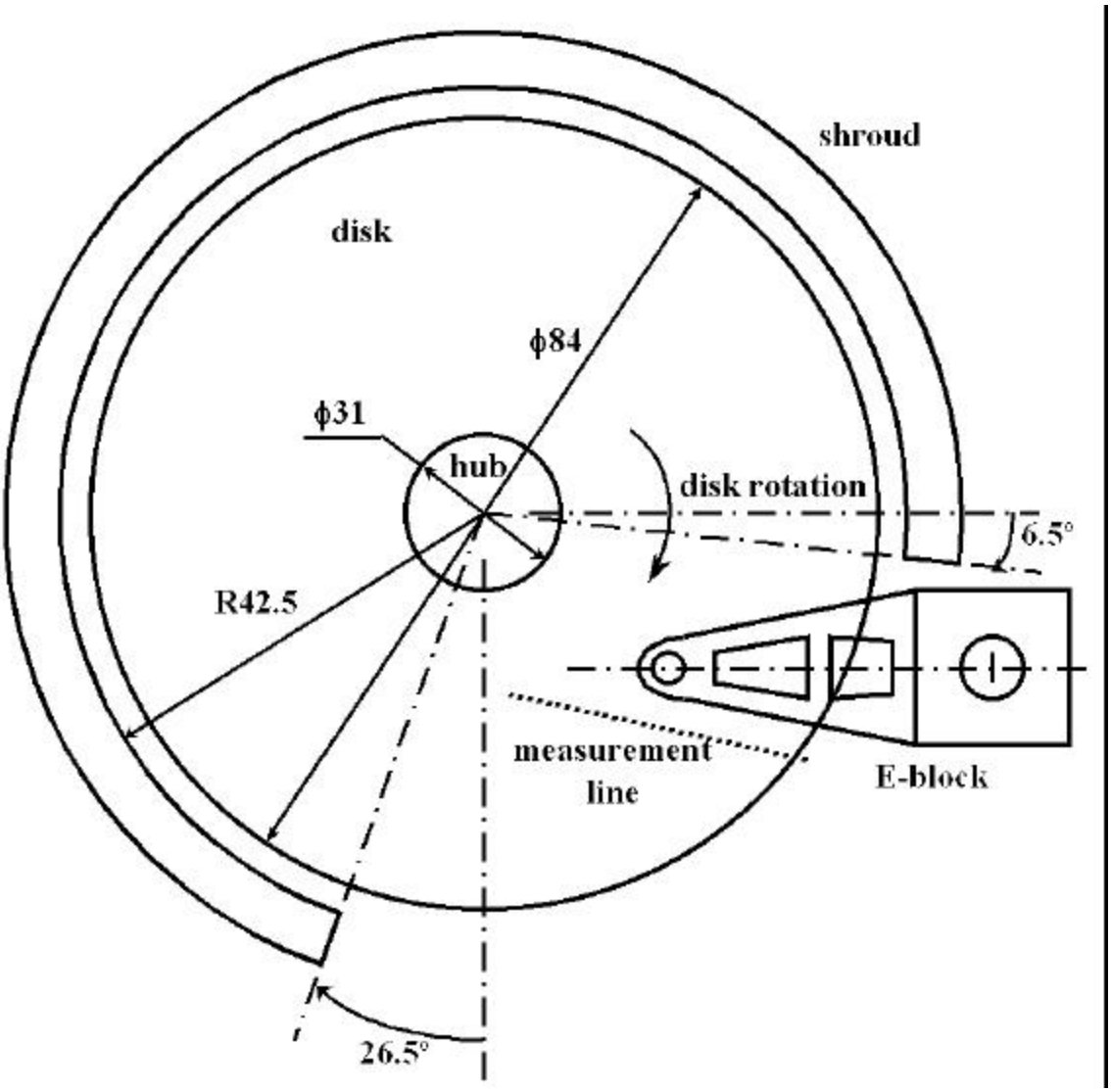


Figure 6: Schematic of setup.

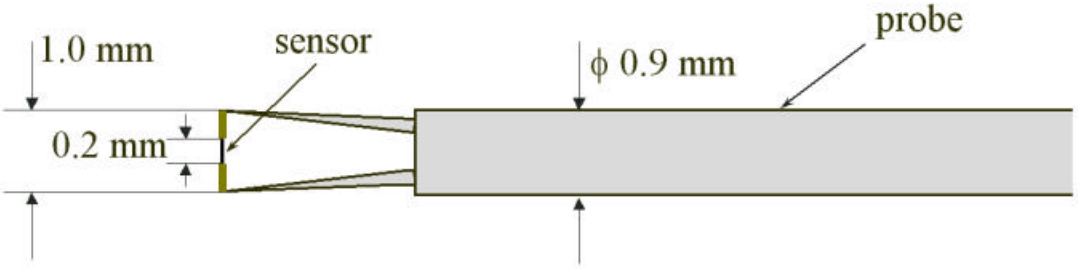


Figure 7: Schematic of hot-wire anemometer.

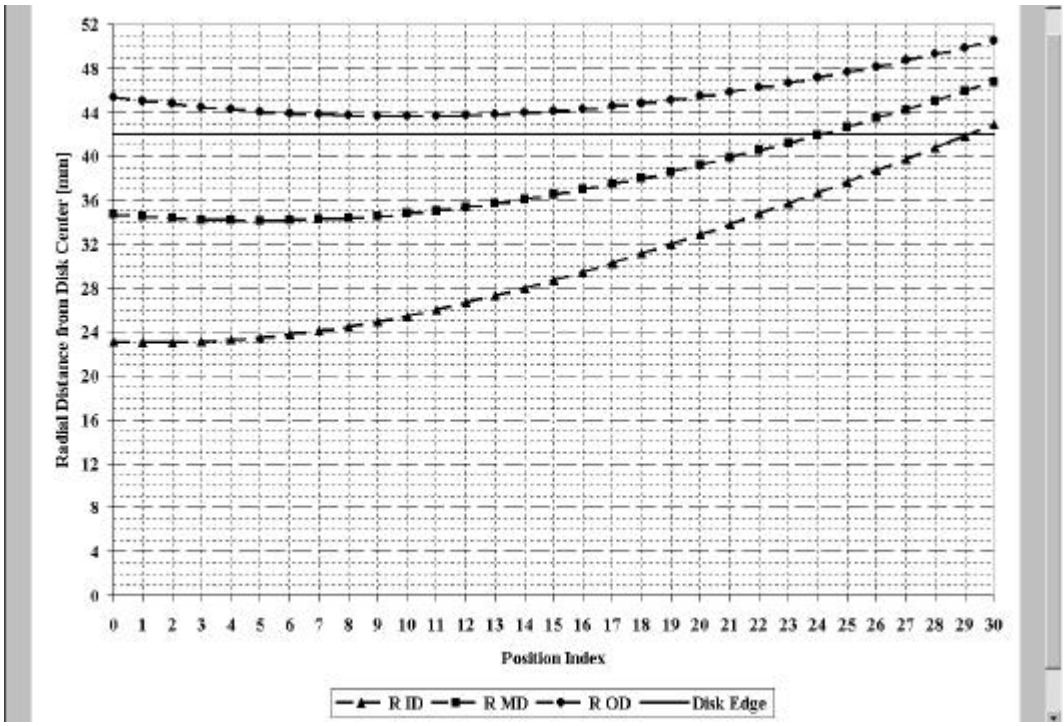


Figure 8: Radial distance of measurement points from disk center; ID, MD, and OD.

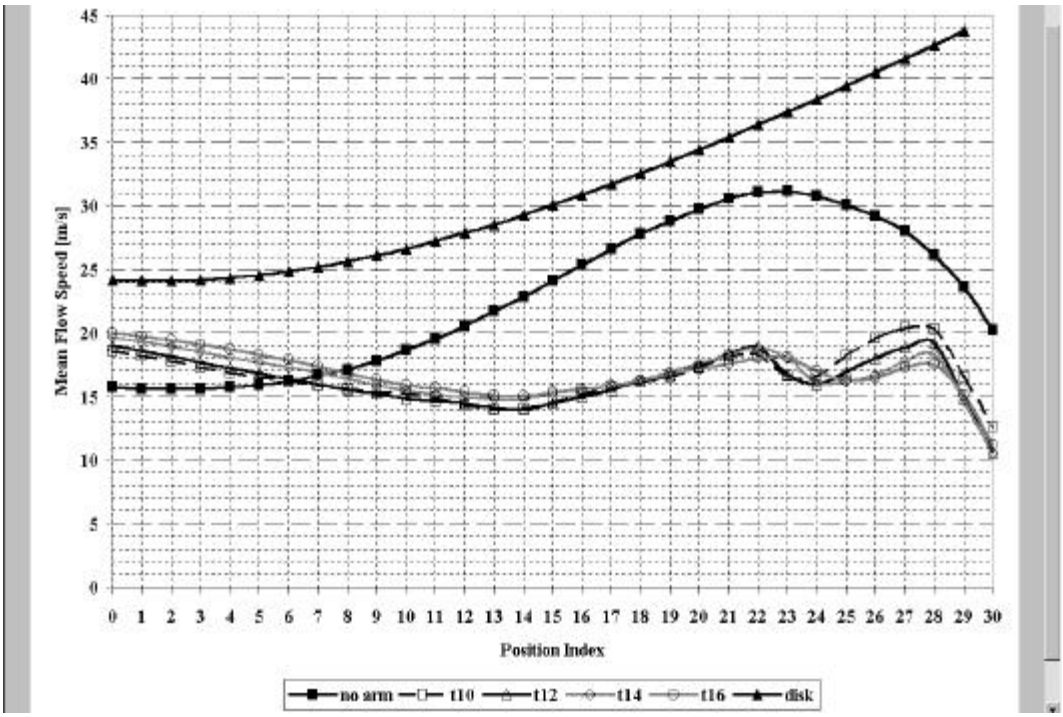


(a) Disk surface speed and unobstructed flow speed profiles shown.

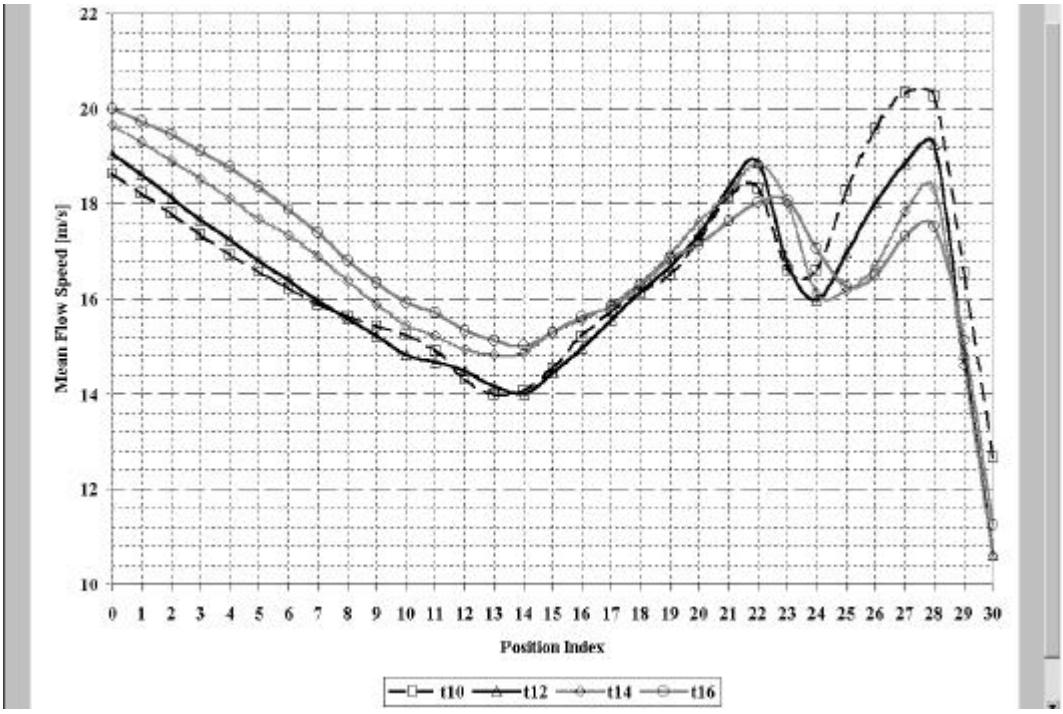


(b) Disk speed and unobstructed flow speed profiles not shown.

Figure 9: Mean flow speed profiles for t10, t12, t14, and t16; ID; “E-block arm”.

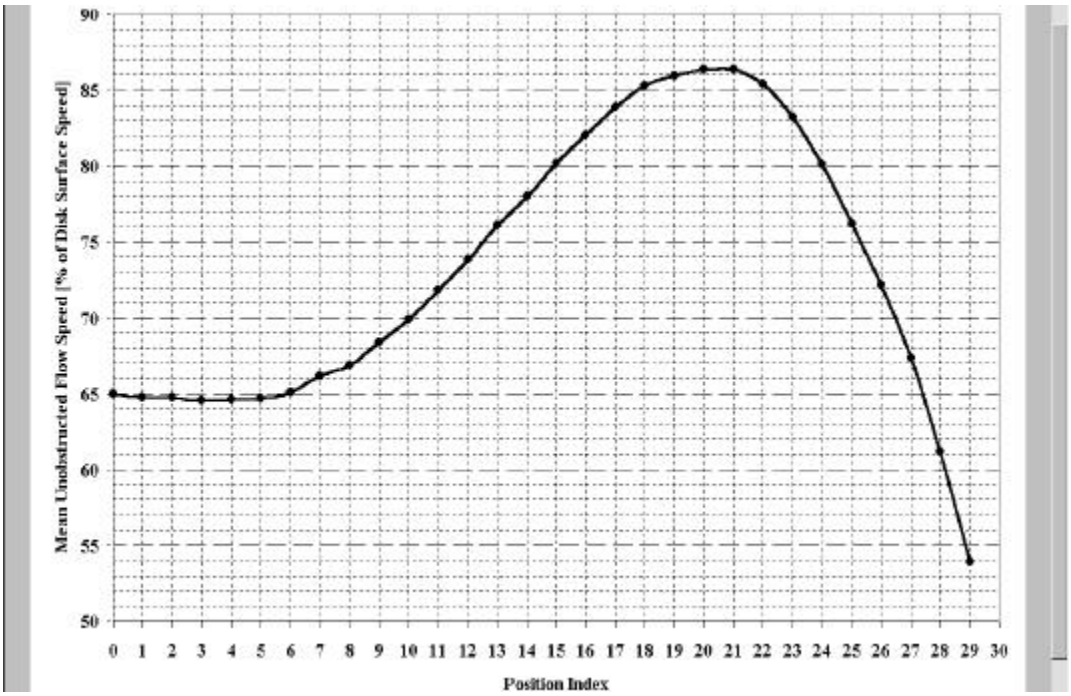


Figure 10: Mean unobstructed flow speed as a percentage of disk surface speed; ID; “E-block arm”.

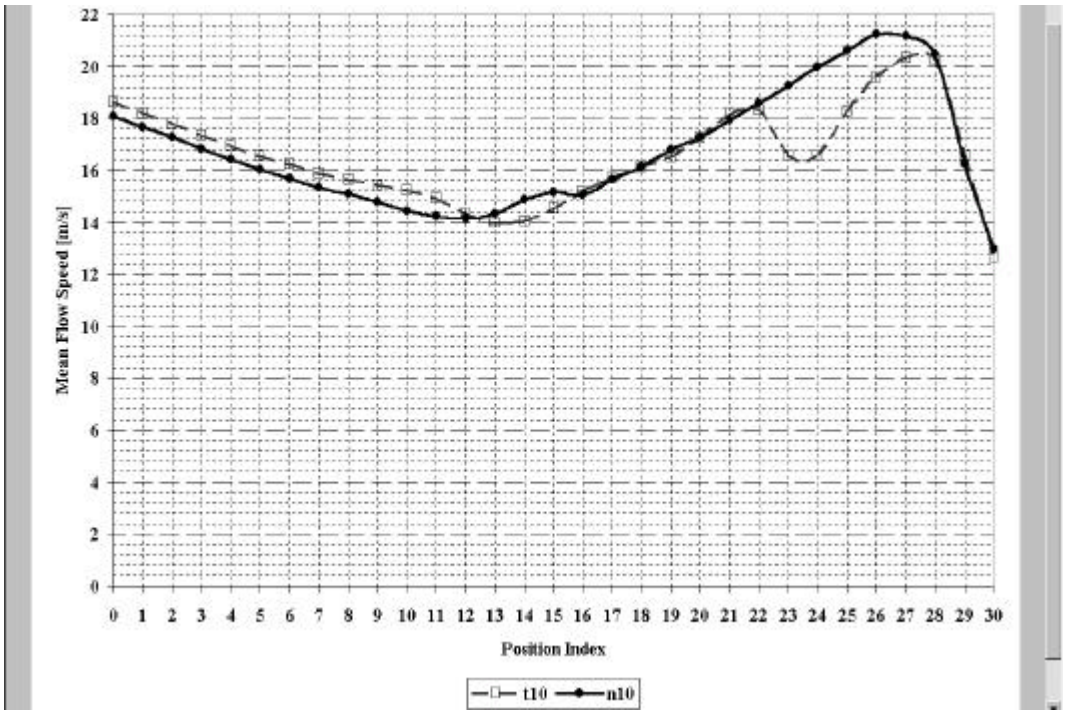


Figure 11: Mean flow speed profiles for t10 and n10; ID; “E-block arm”.

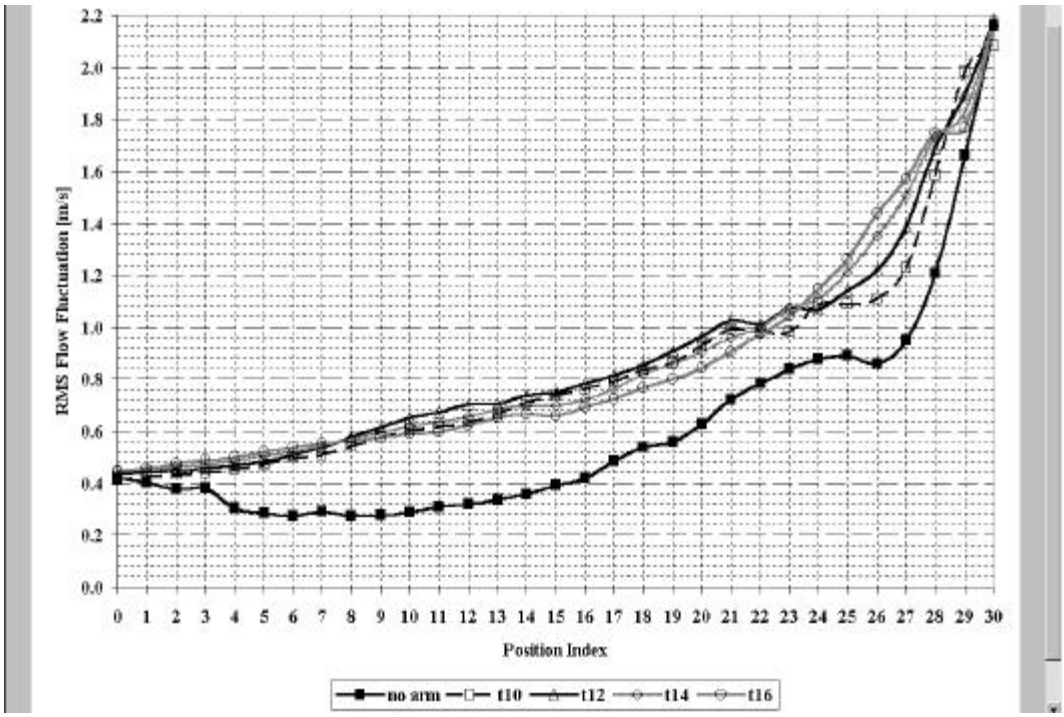


Figure 12: RMS flow fluctuation profiles for unobstructed flow, t10, t12, t14, and t16; ID; “E-block arm”.

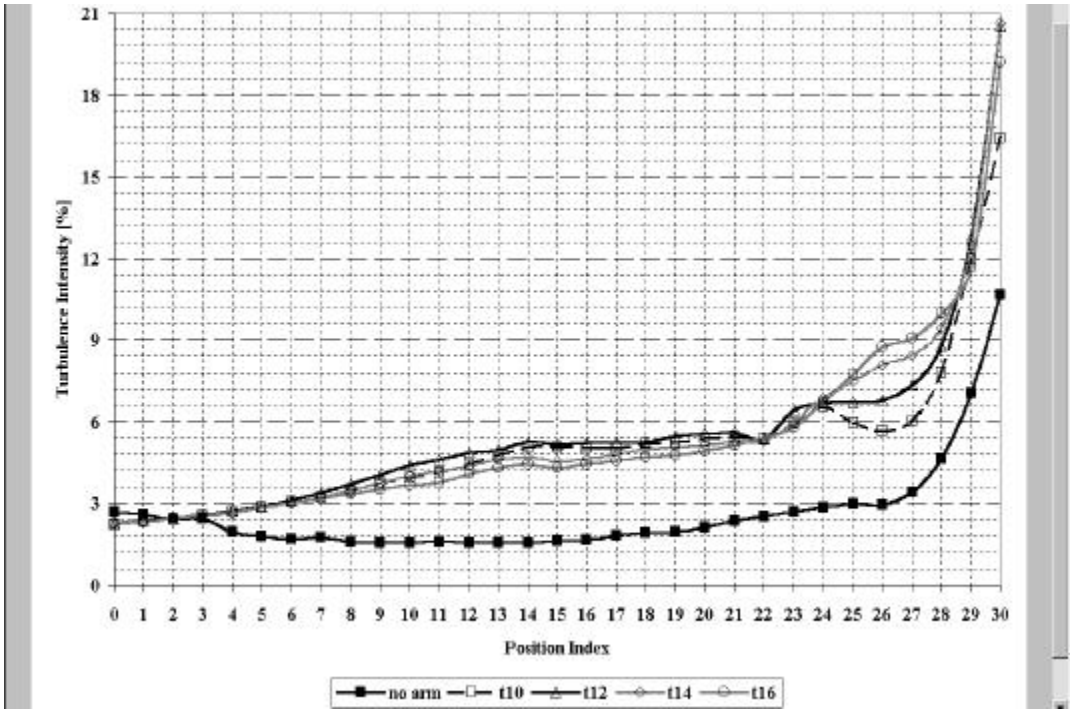


Figure 13: Turbulence intensity profiles for unobstructed flow, t10, t12, t14, and t16; ID; “E-block arm”.

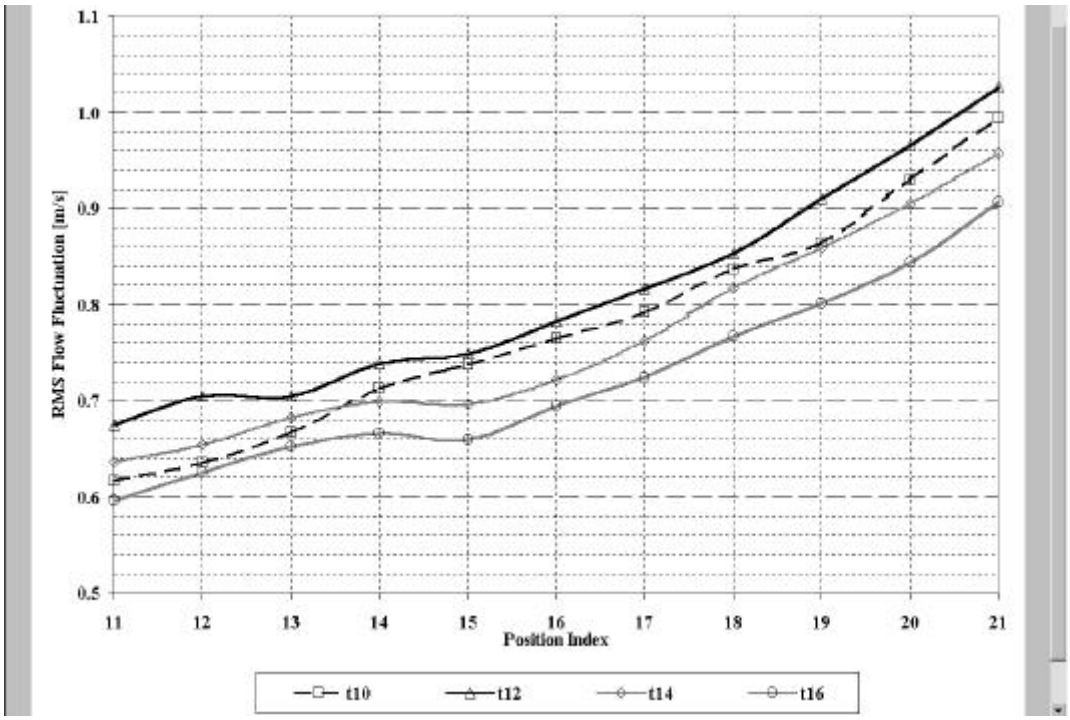


(a) RMS flow fluctuation profiles downstream of arm tip.

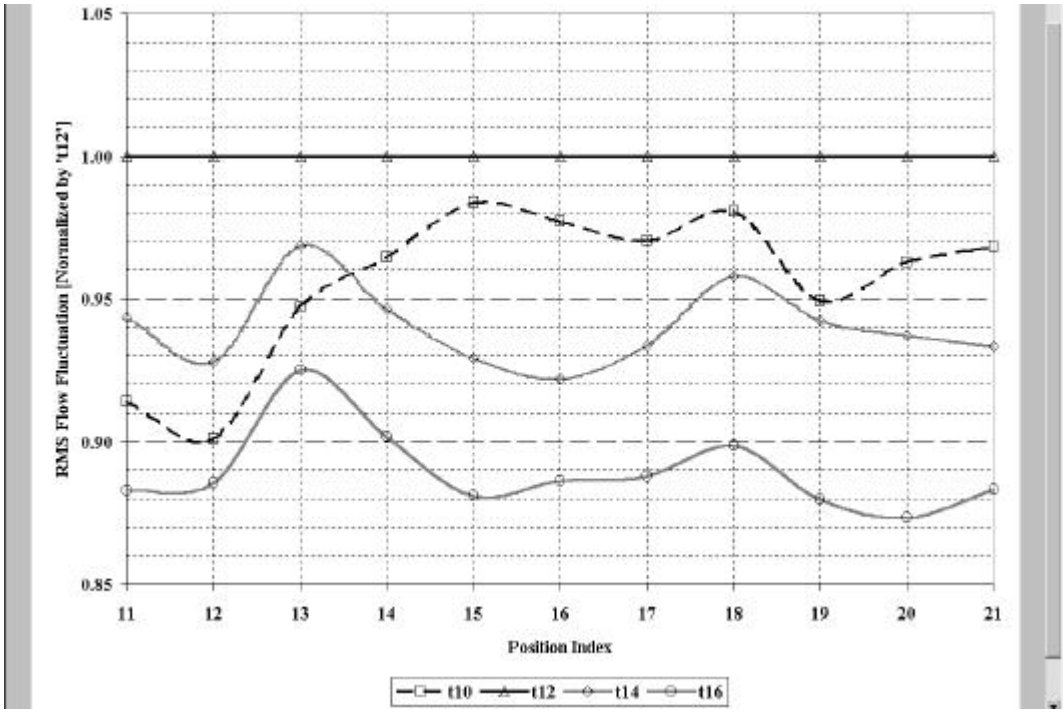


(b) RMS flow fluctuation profiles downstream of arm tip, normalized by 't12'.

Figure 14: RMS flow fluctuation profiles downstream of arm tip; ID; "E-block arm".

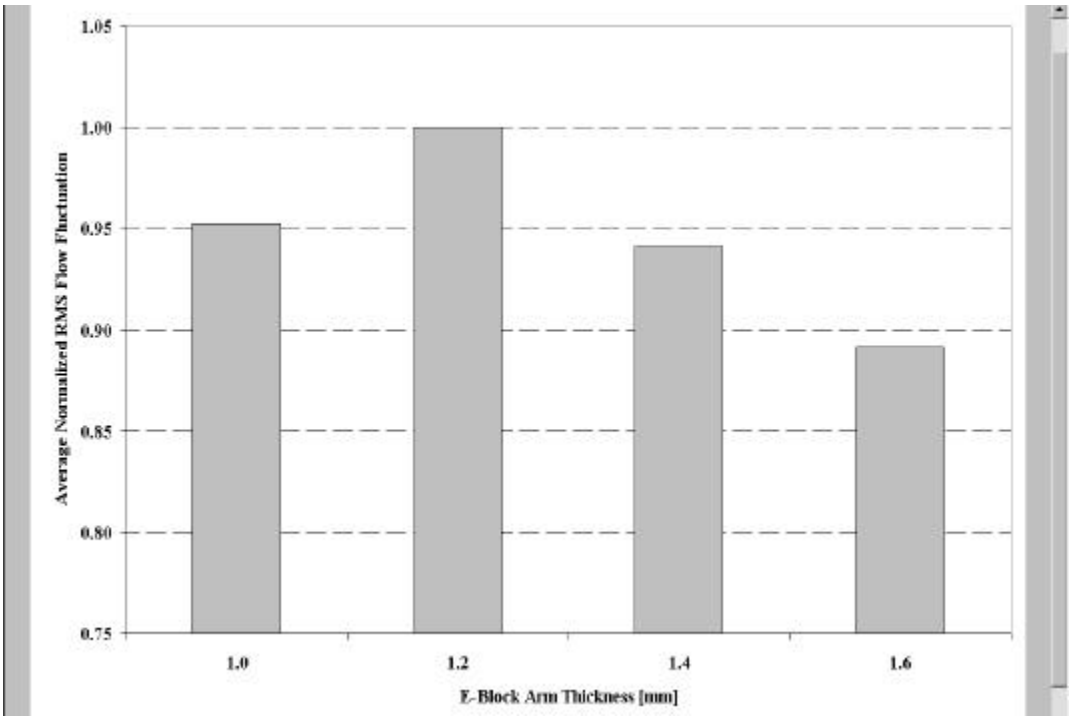


Figure 15: Average normalized flow fluctuation vs. arm thickness; ID; “E-block arm”.

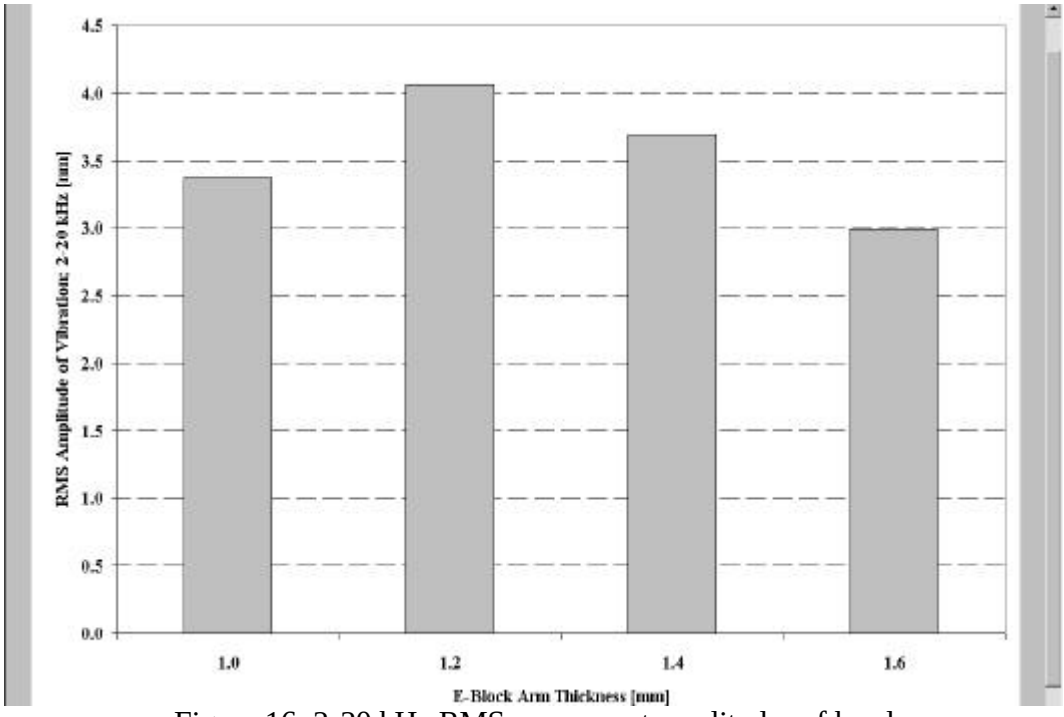


Figure 16: 2-20 kHz RMS component amplitudes of head off-track vibration vs. arm thickness; ID.

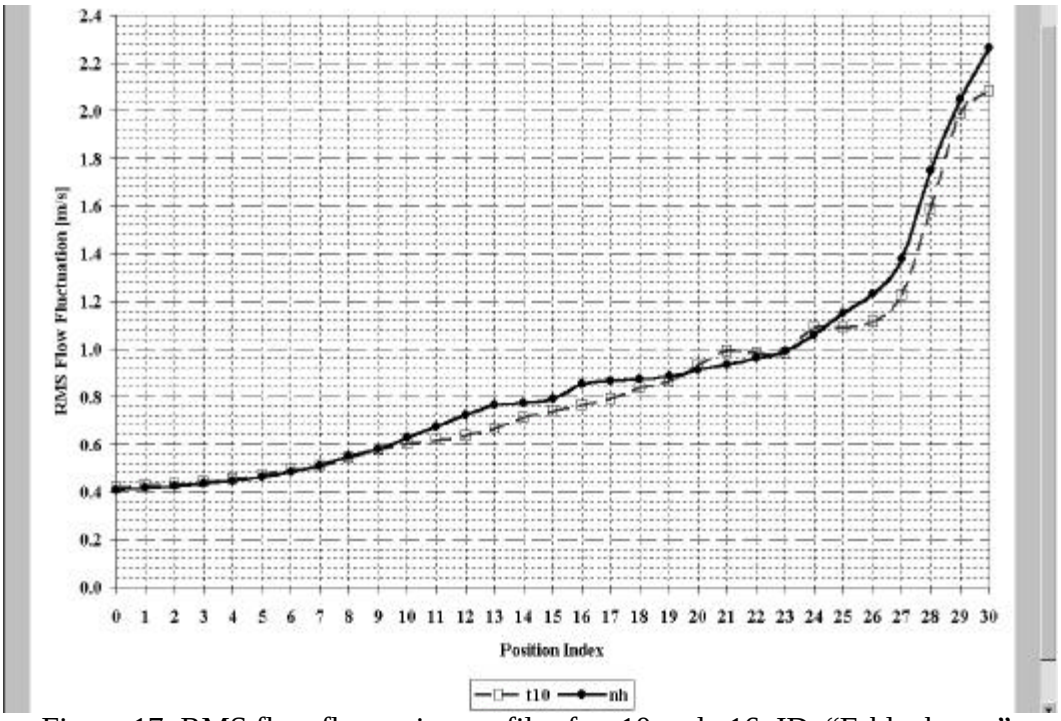


Figure 17: RMS flow fluctuation profiles for t10 and n16; ID; “E-block arm”.

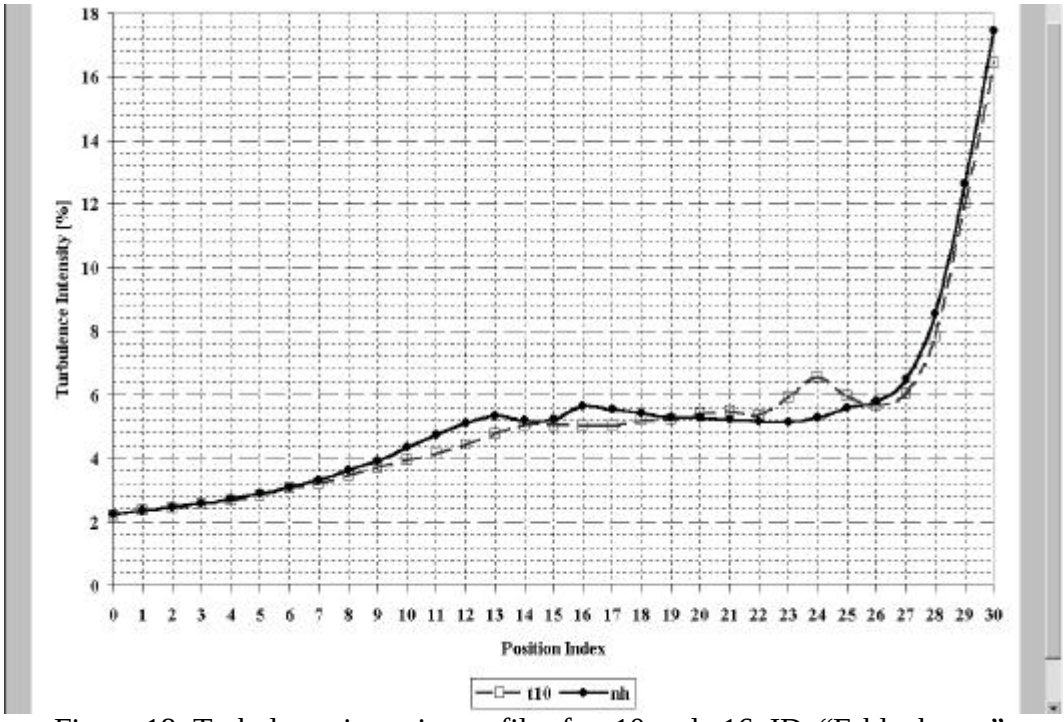


Figure 18: Turbulence intensity profiles for t10 and n16; ID; “E-block arm”.

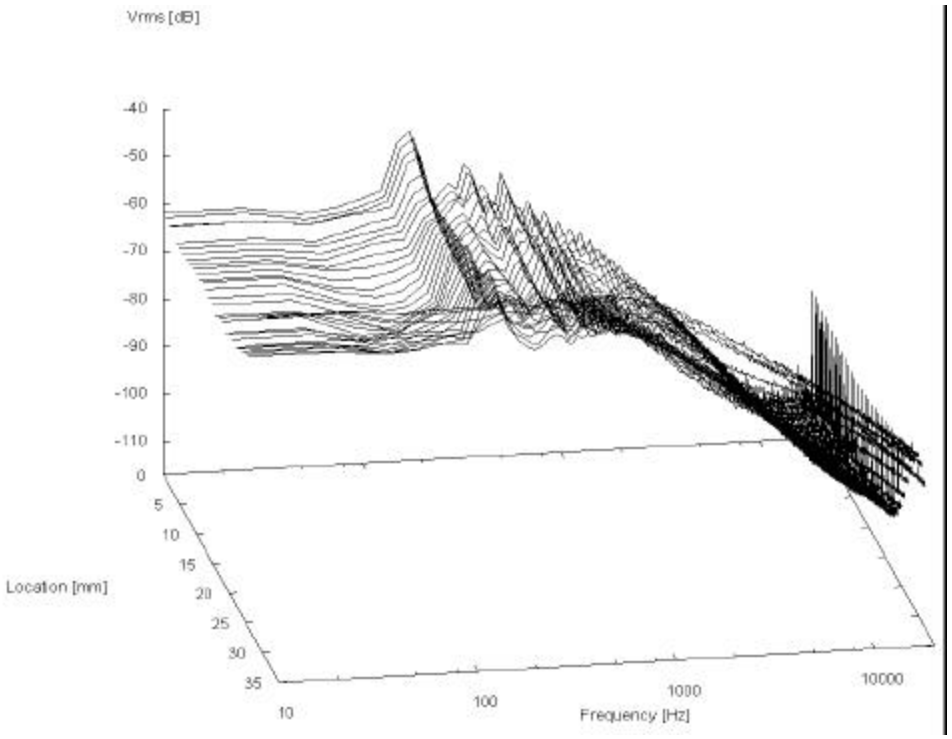


Figure 19: Power spectra of flow fluctuation; unobstructed flow; ID; “E-block arm”.

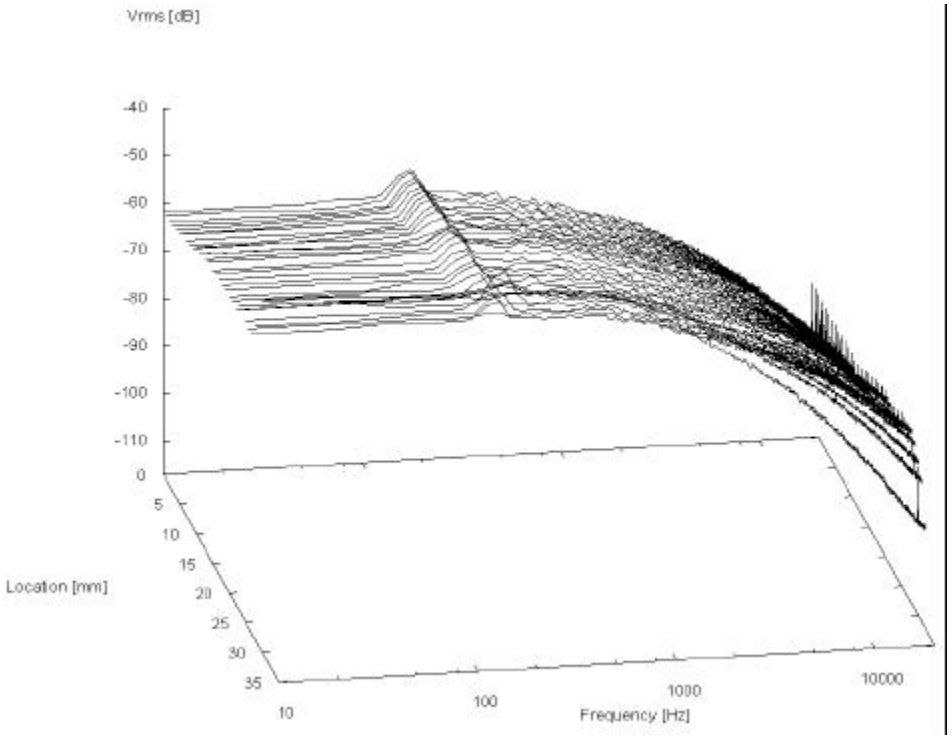


Figure 20: Power spectra of flow fluctuation; t10; ID; “E-block arm”.

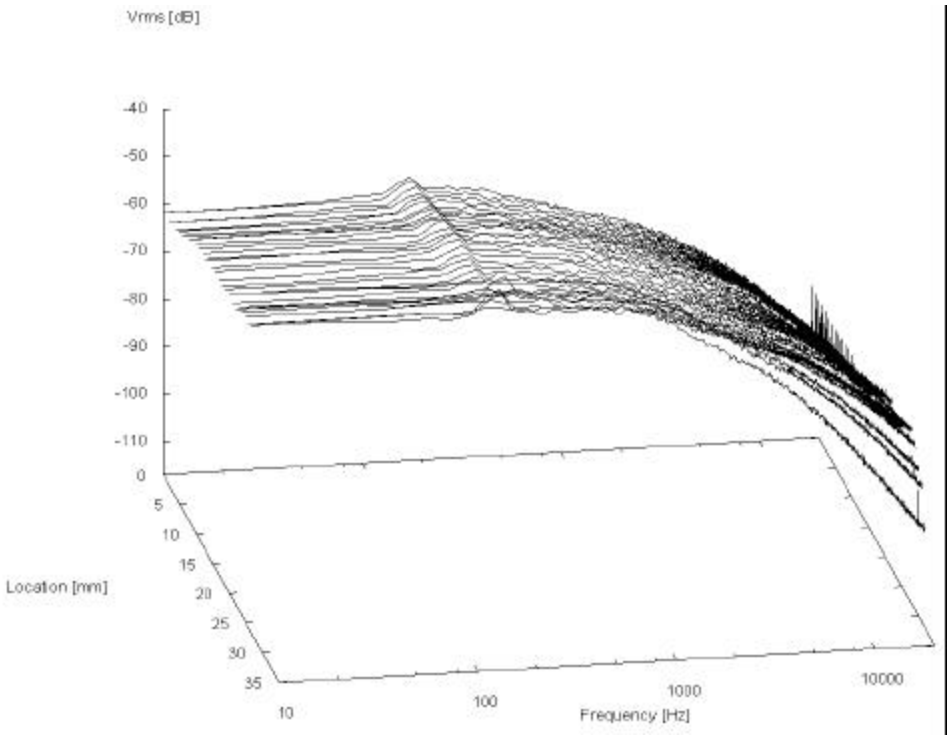

Figure 21: Power spectra of flow fluctuation; t12; ID; “E-block arm”.

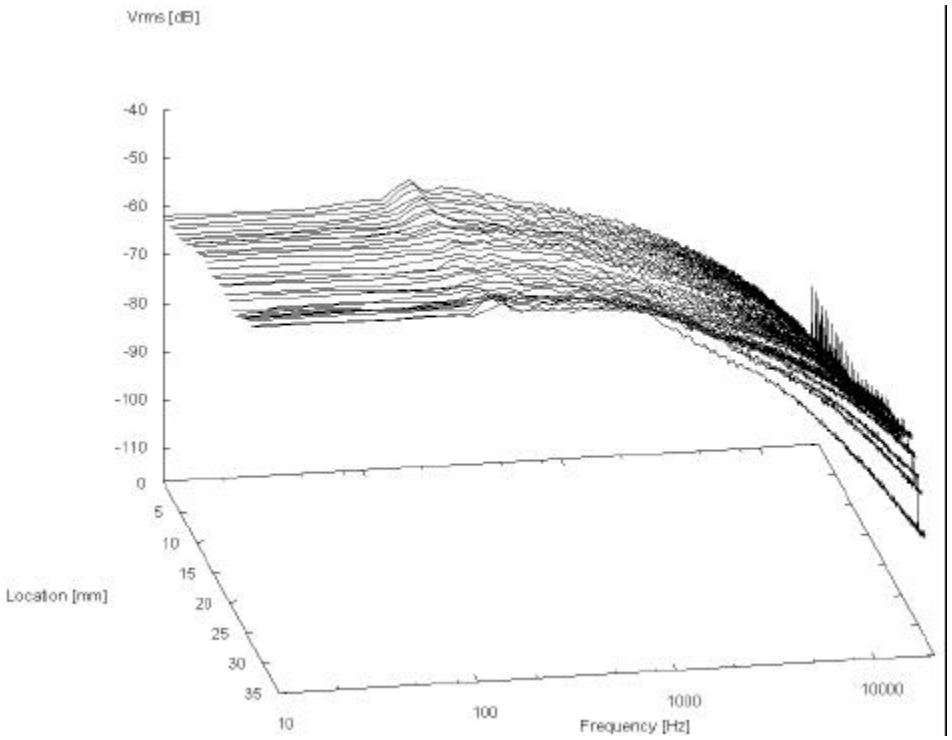

Figure 22: Power spectra of flow fluctuation; t14; ID; “E-block arm”.

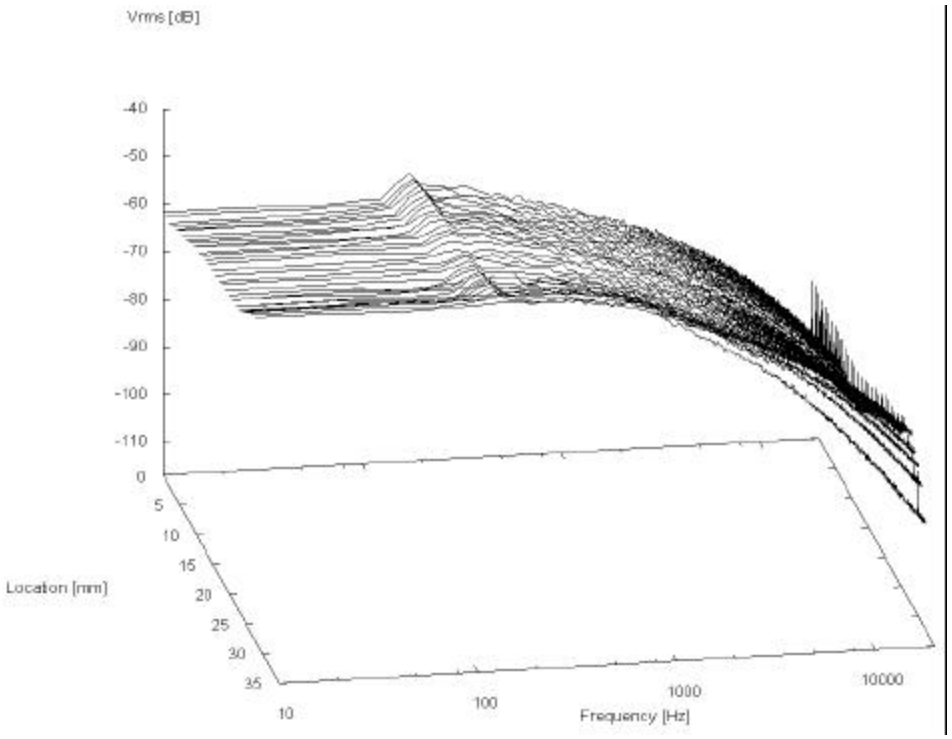


Figure 23: Power spectra of flow fluctuation; t16; ID; “E-block arm”.

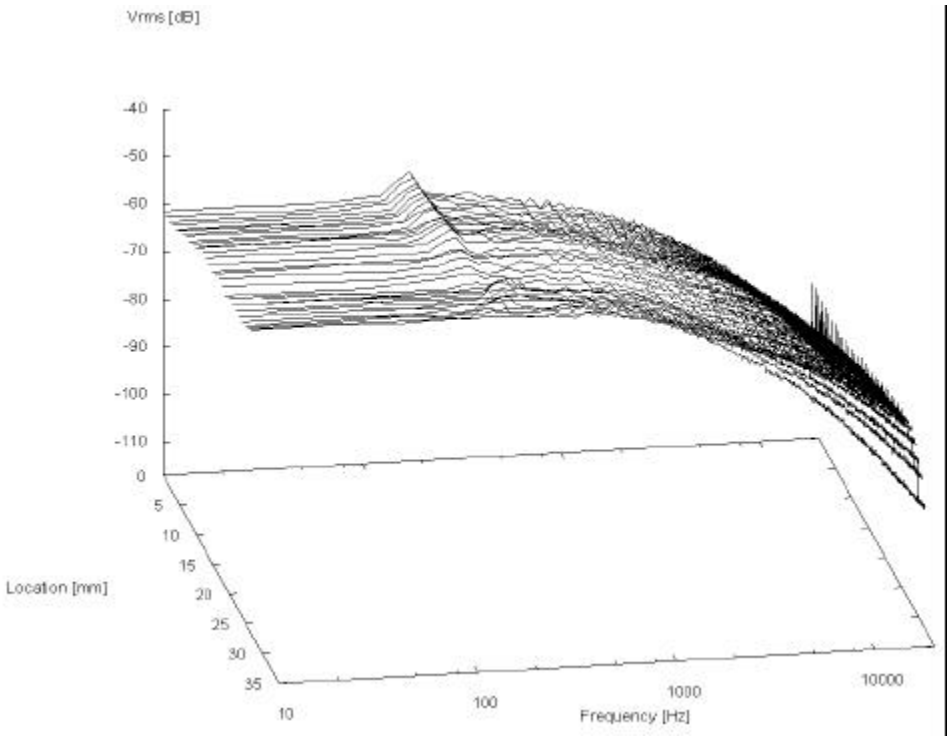


Figure 24: Power spectra of flow fluctuation; n10; ID; “E-block arm”.

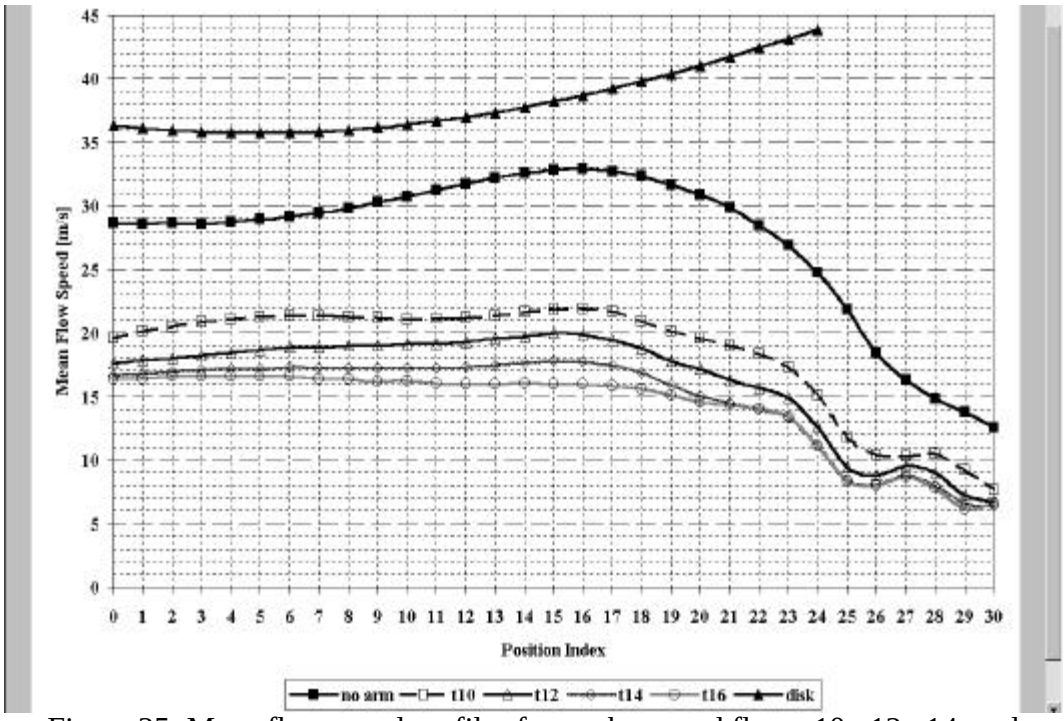


Figure 25: Mean flow speed profiles for unobstructed flow, t10, t12, t14, and t16; MD; “E-block arm”. Disk surface speed profile shown.

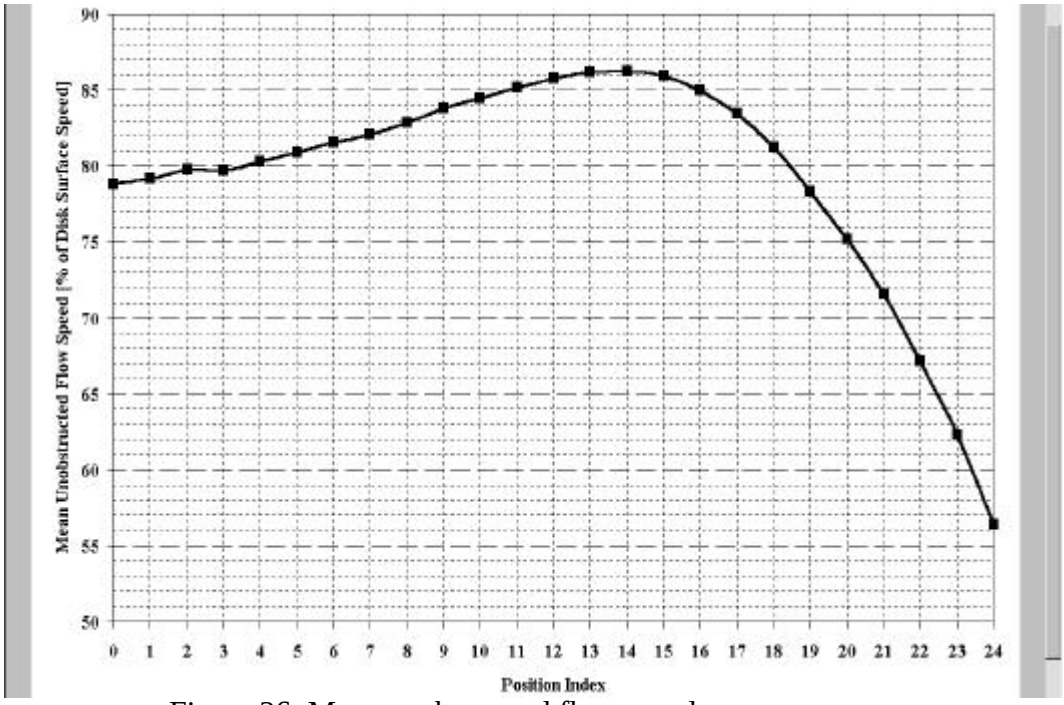


Figure 26: Mean unobstructed flow speed as a percentage of disk surface speed; MD; “E-block arm”.

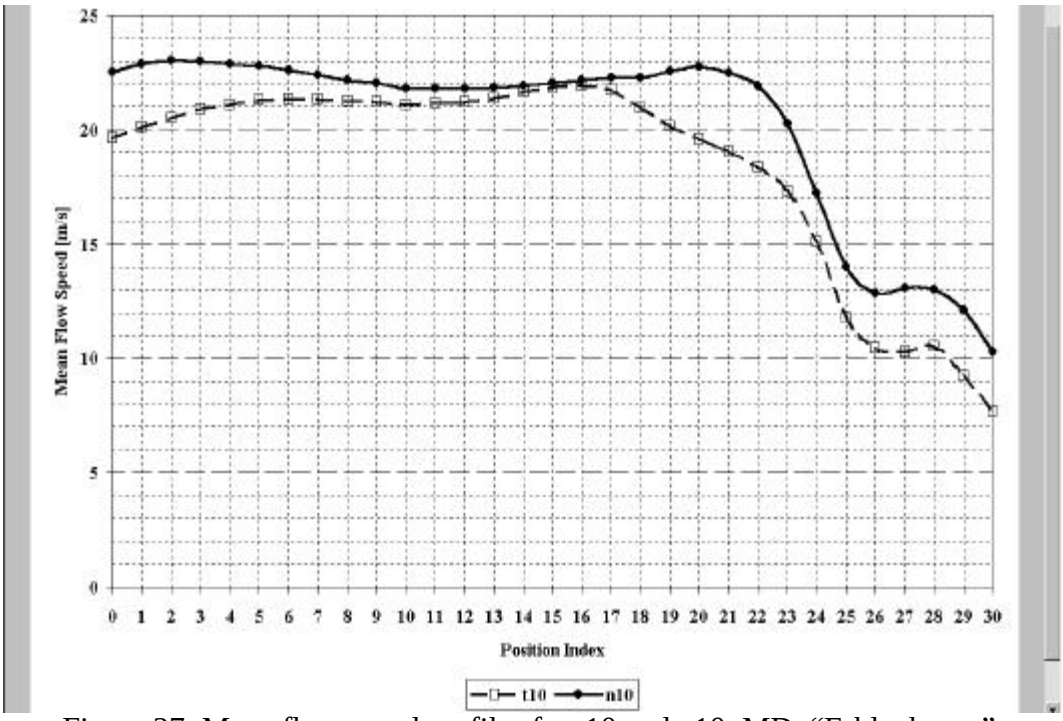


Figure 27: Mean flow speed profiles for t10 and n10; MD; “E-block arm”.

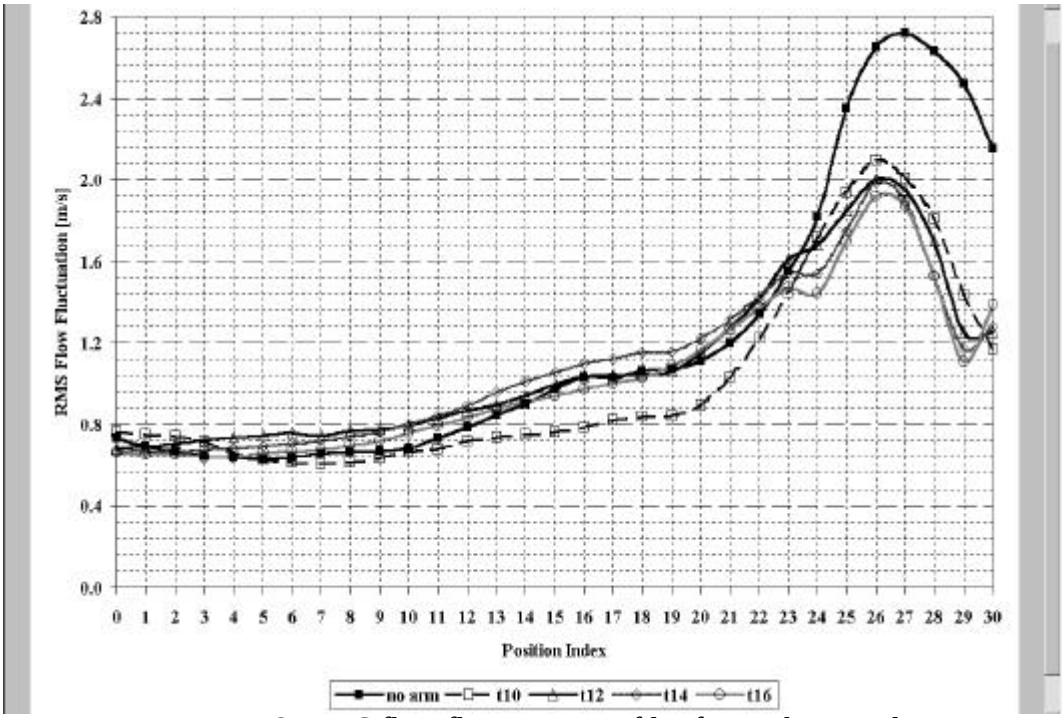


Figure 28: RMS flow fluctuation profiles for unobstructed flow, t10, t12, t14, and t16; MD; “E-block arm”.

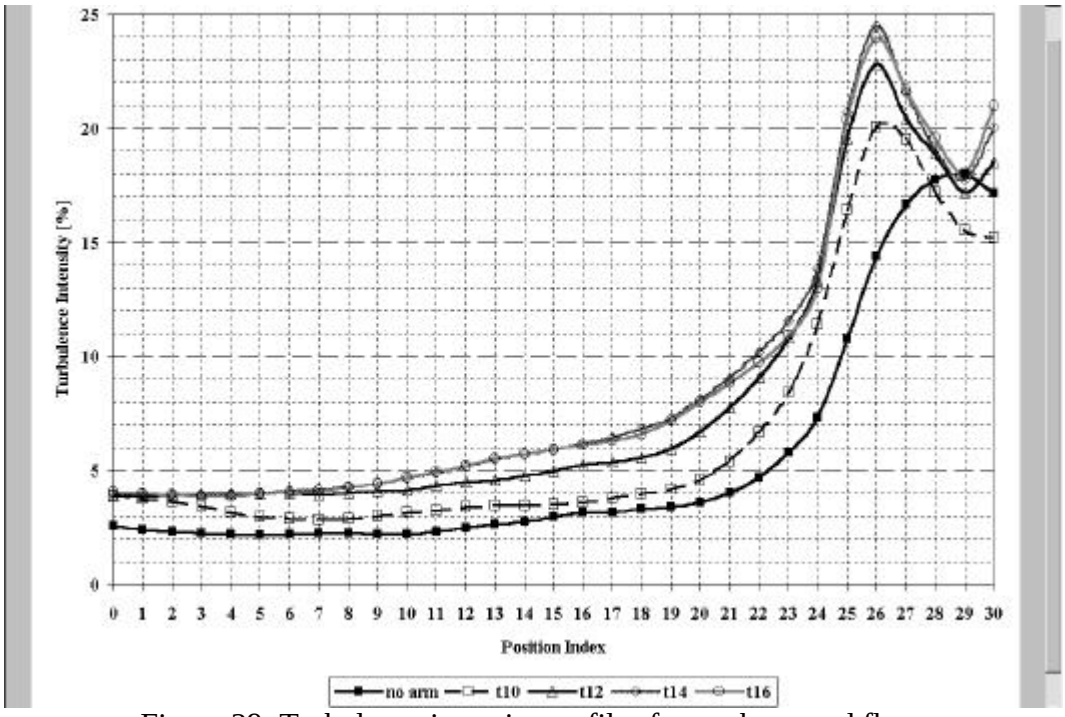


Figure 29: Turbulence intensity profiles for unobstructed flow, t10, t12, t14, and t16; MD; “E-block arm”.

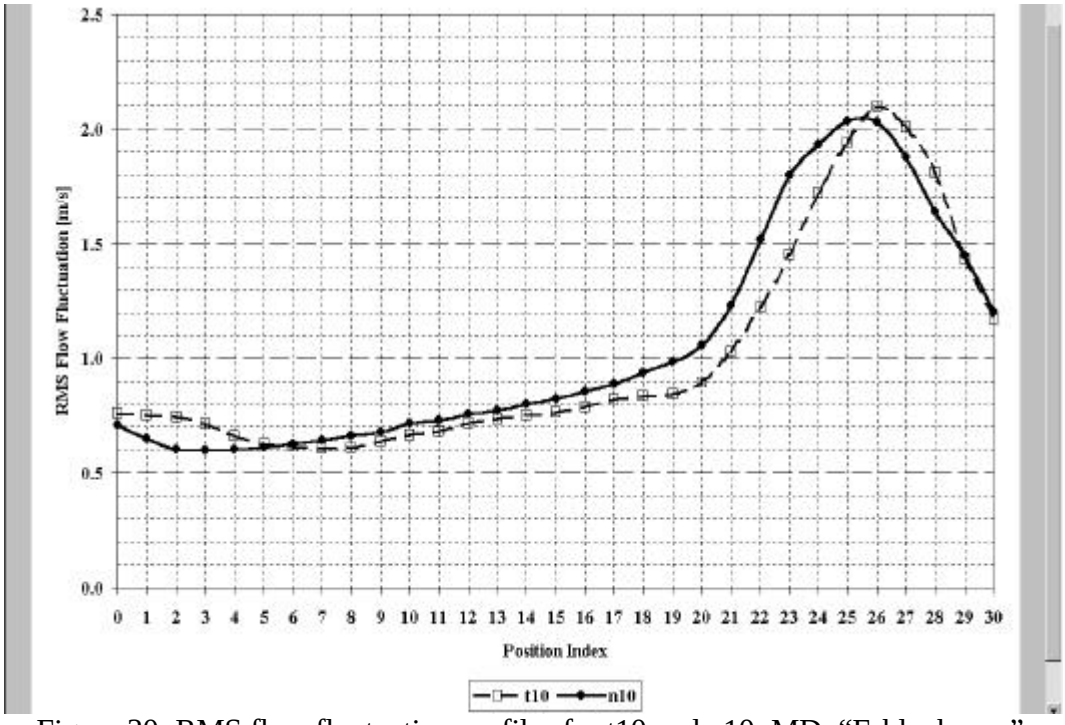


Figure 30: RMS flow fluctuation profiles for t10 and n10; MD; “E-block arm”.

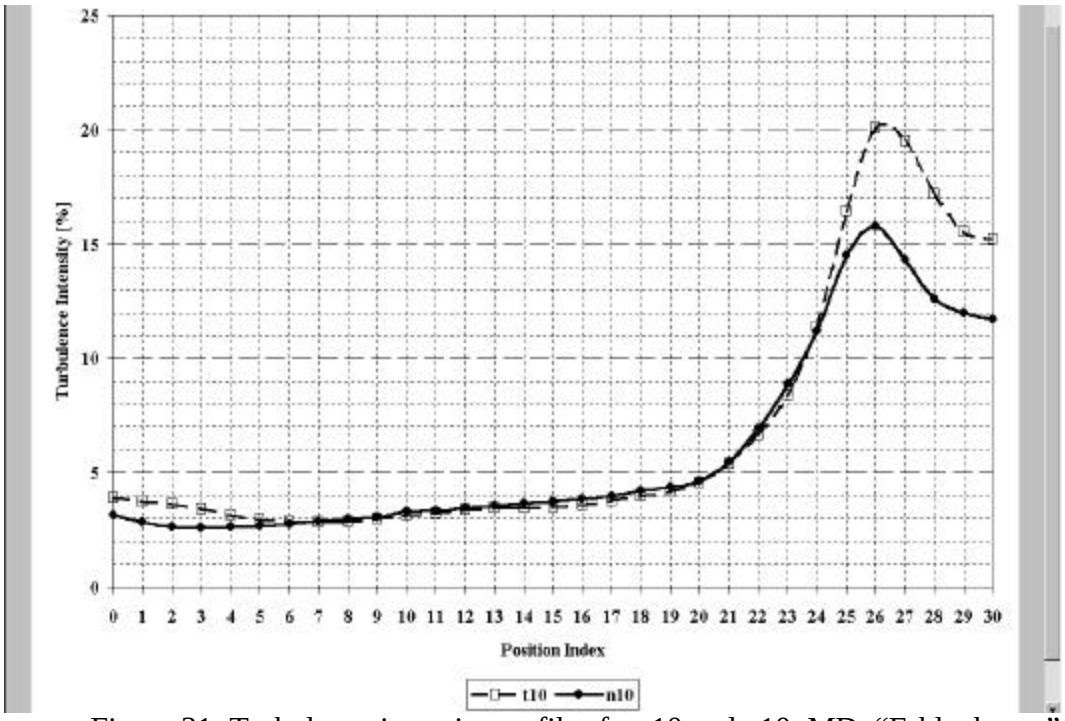

Figure 31: Turbulence intensity profiles for t10 and n10; MD; “E-block arm”.

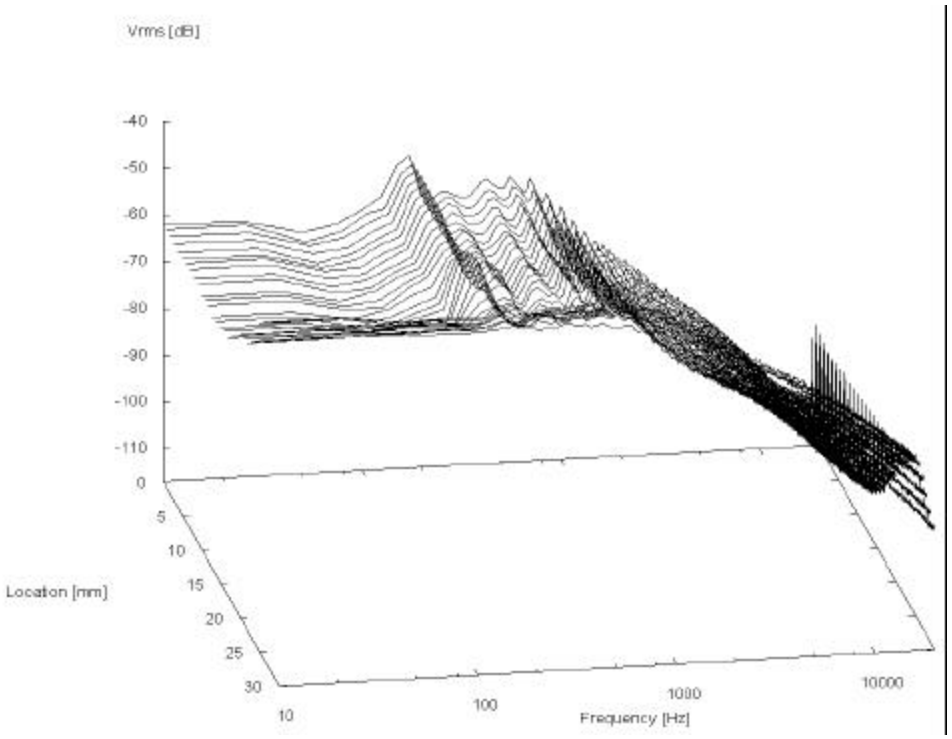


Figure 32: Power spectra of flow fluctuation; unobstructed flow; MD; “E-block arm”.

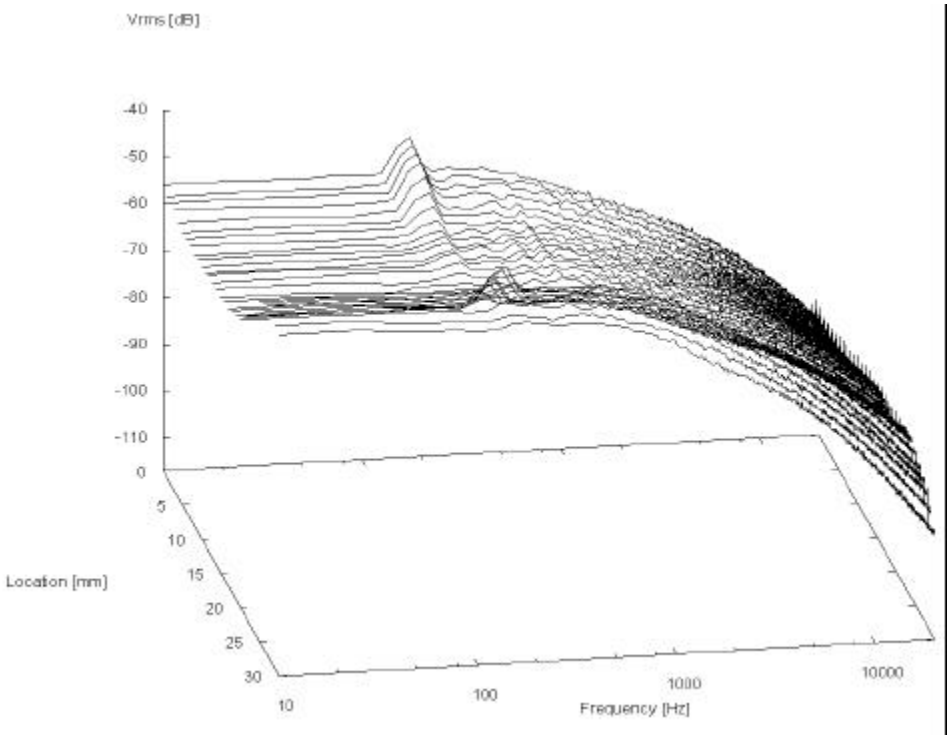


Figure 33: Power spectra of flow fluctuation; t10; MD; “E-block arm”.

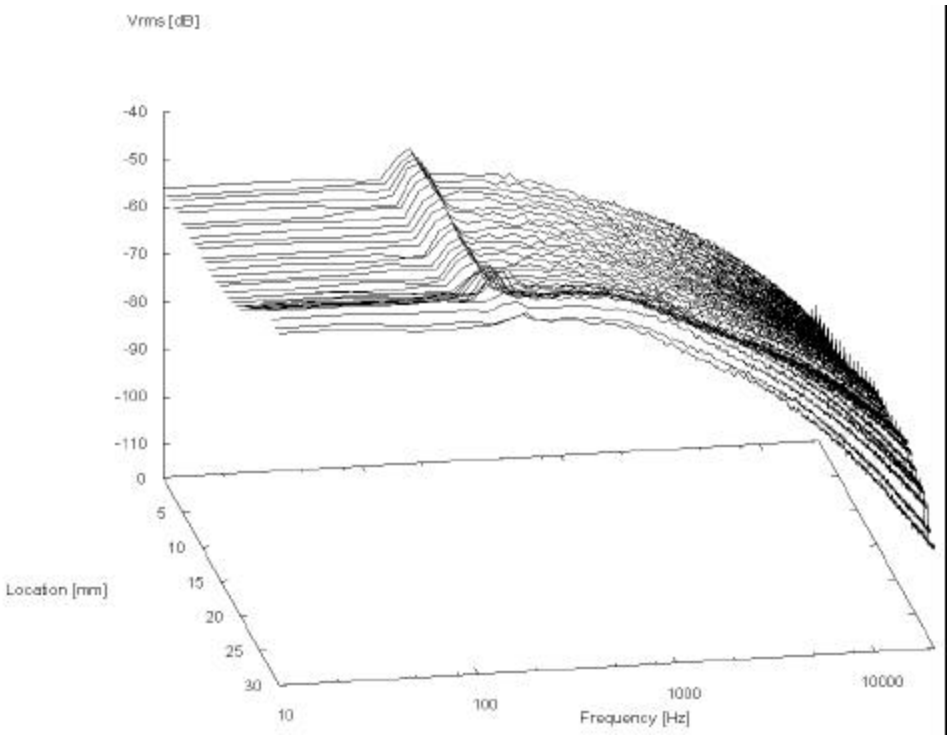

Figure 34: Power spectra of flow fluctuation; t12; MD; “E-block arm”.

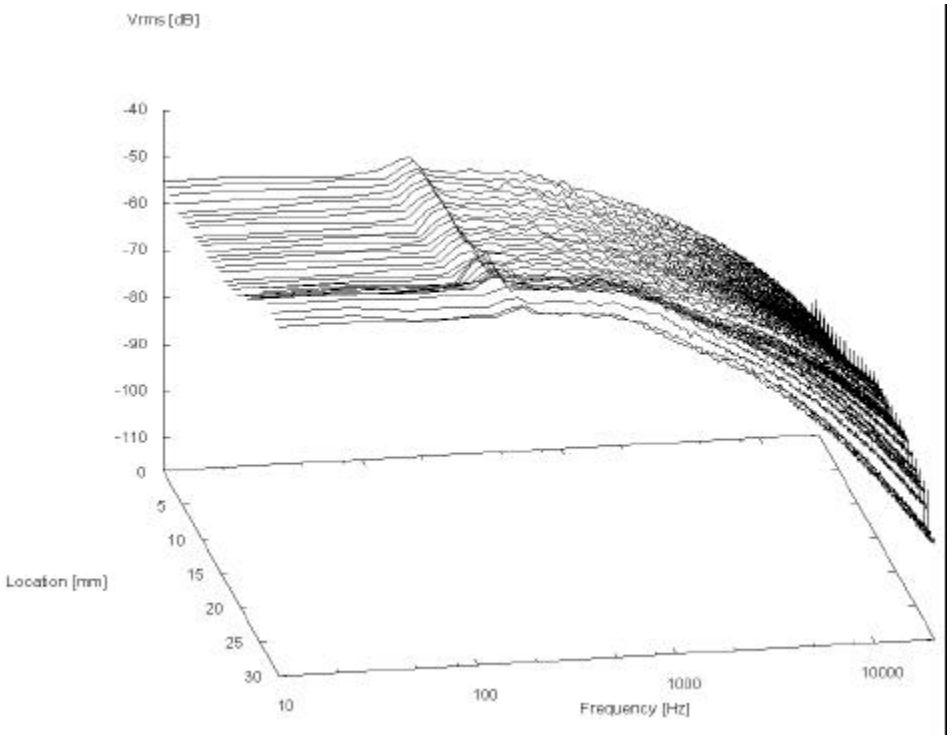

Figure 35: Power spectra of flow fluctuation; t14; MD; “E-block arm”.

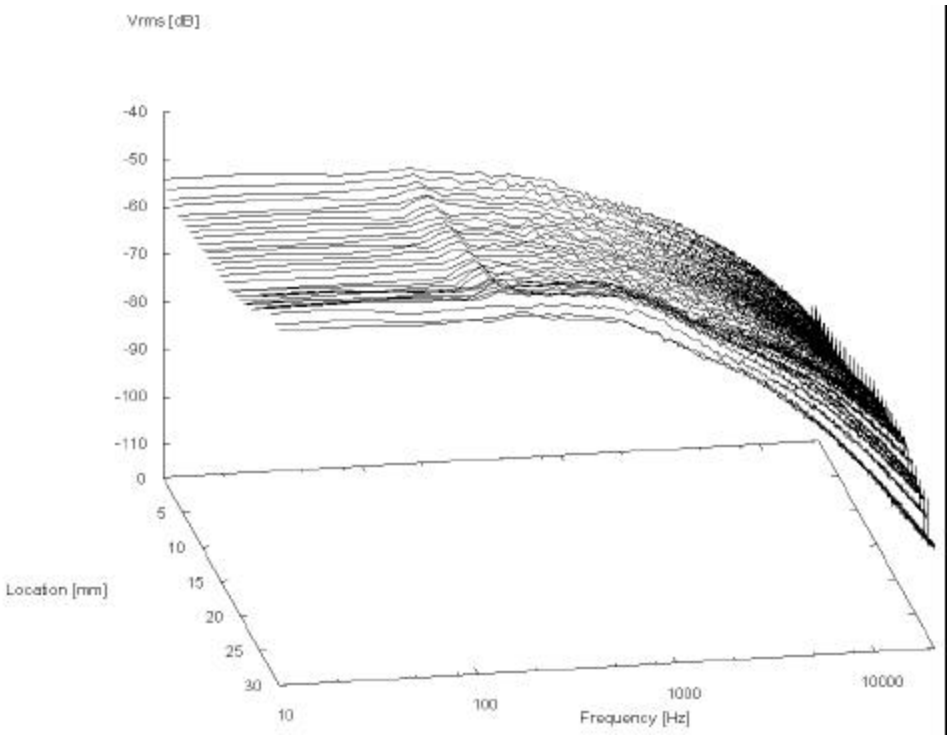


Figure 36: Power spectra of flow fluctuation; t16; MD; “E-block arm”.

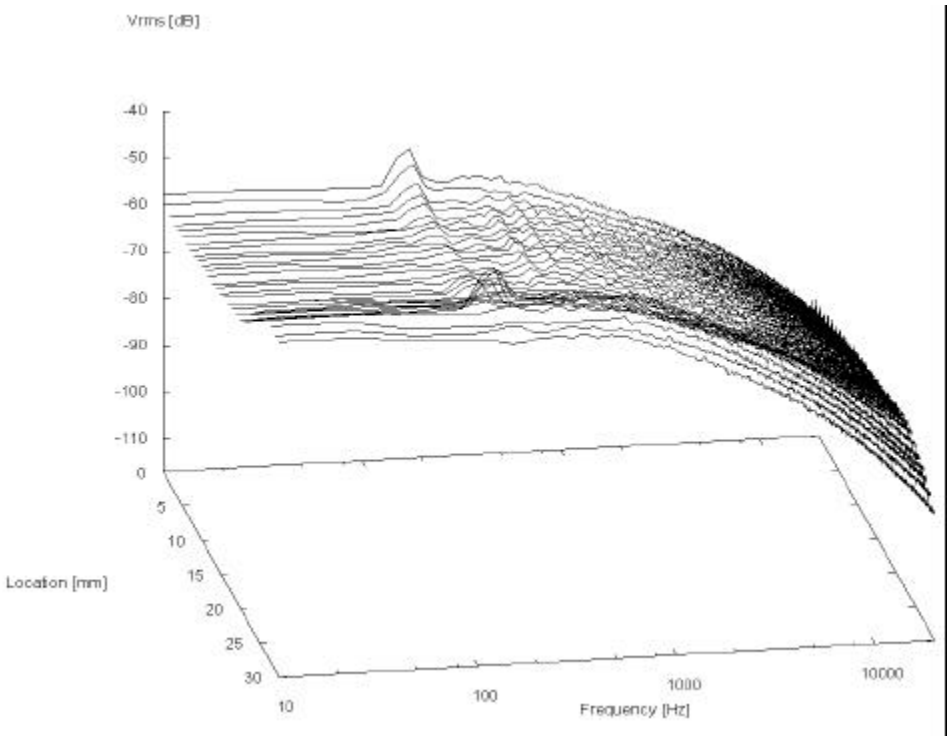


Figure 37: Power spectra of flow fluctuation; n10; MD; “E-block arm”.

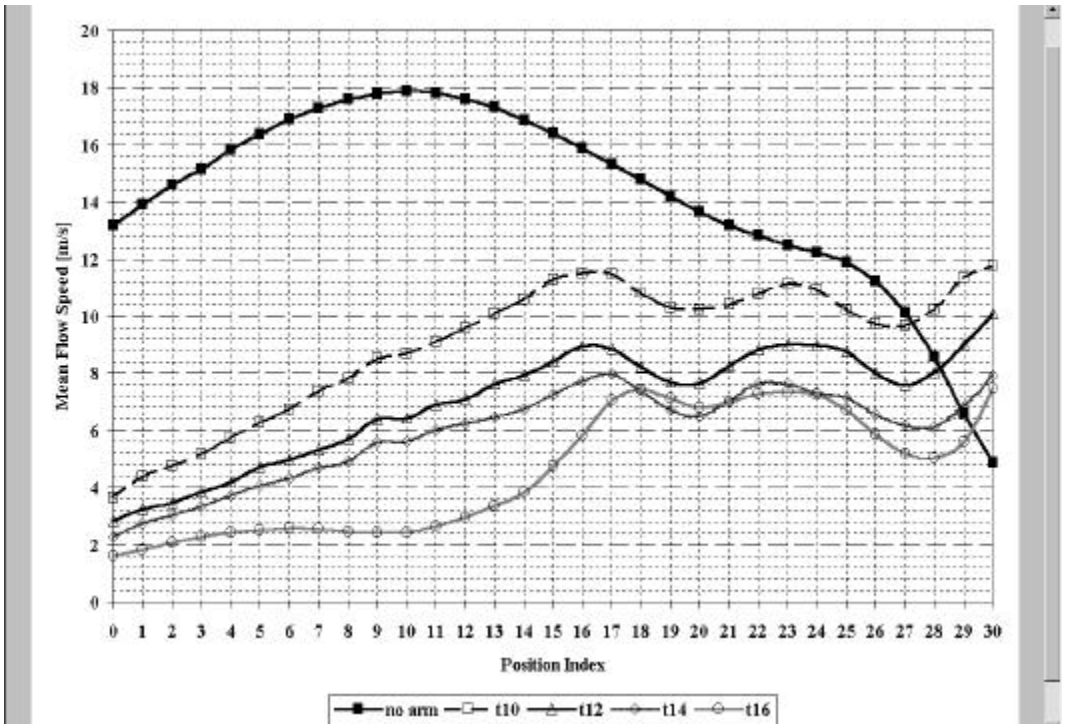


Figure 38: Mean flow speed profiles for unobstructed flow, t10, t12, t14, and t16; OD; “E-block arm”.

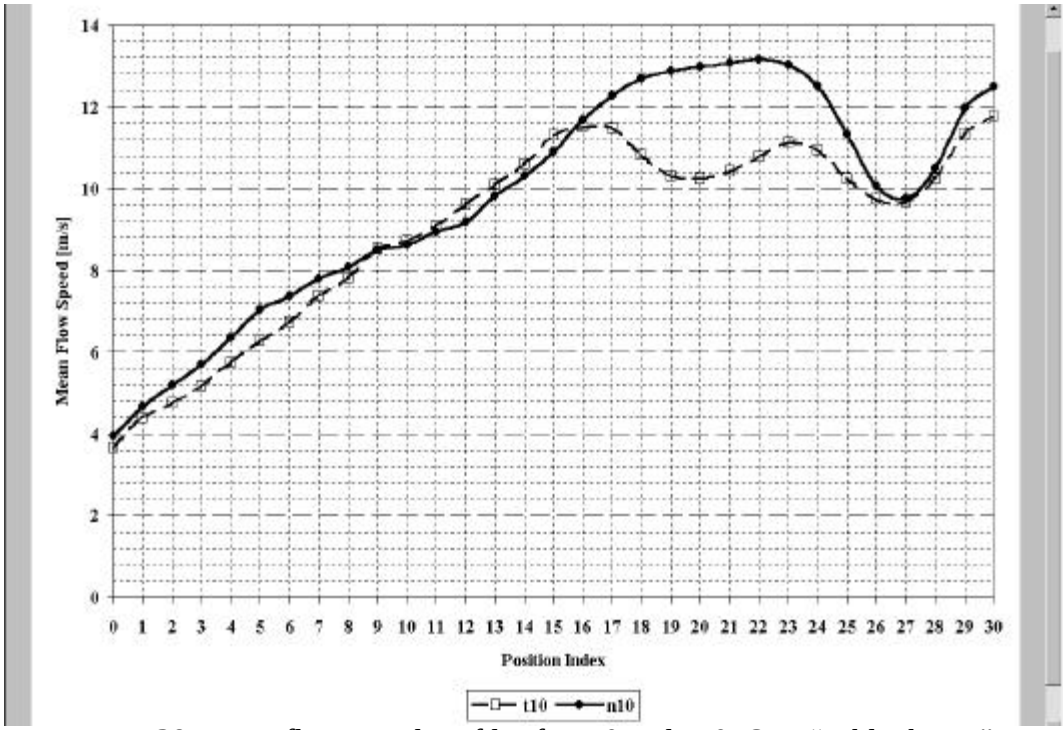


Figure 39: Mean flow speed profiles for t10 and n10; OD; “E-block arm”.

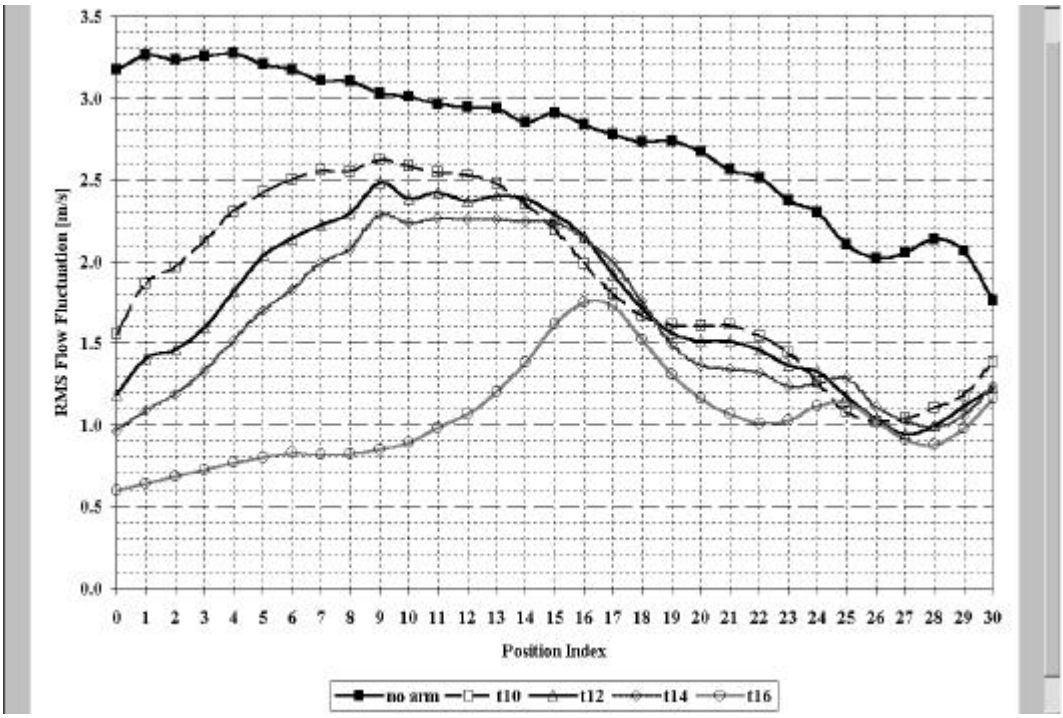


Figure 40: RMS flow fluctuation profiles for unobstructed flow, t10, t12, t14, and t16; OD; “E-block arm”.

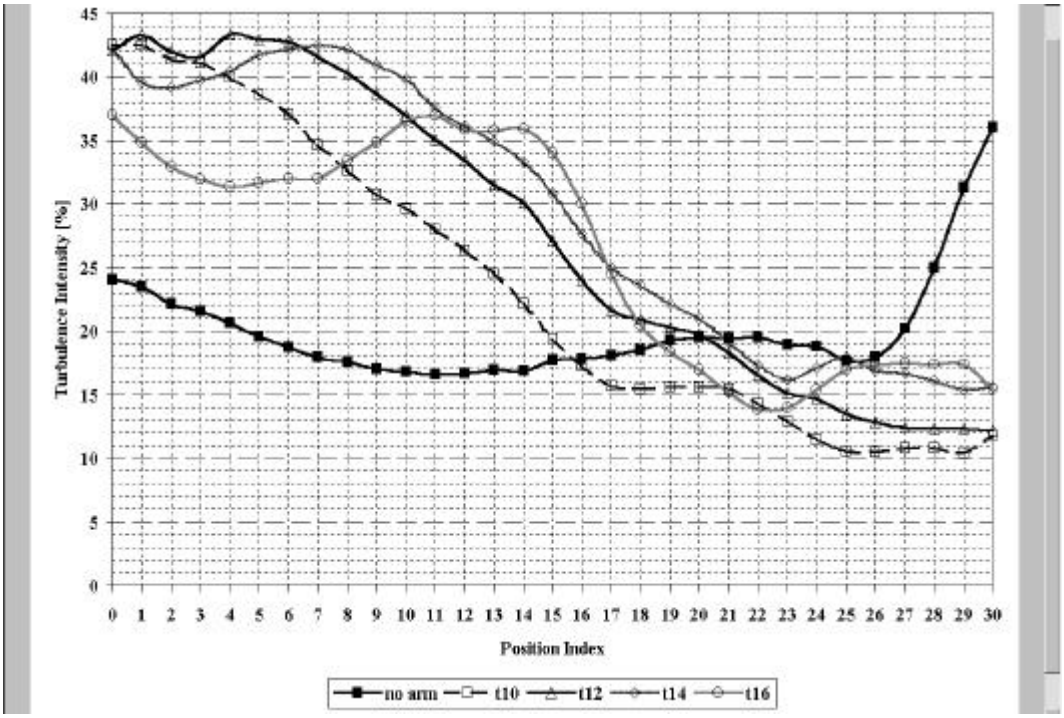


Figure 41: Turbulence intensity profiles for unobstructed flow, t10, t12, t14, and t16; OD; “E-block arm”.

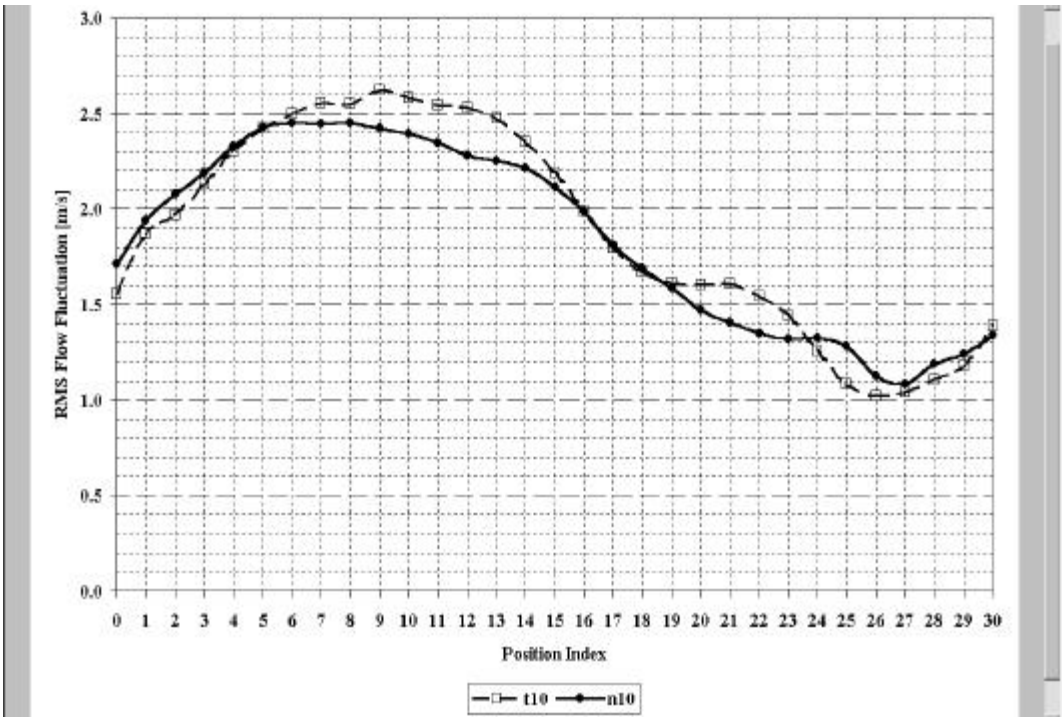

Figure 42: RMS flow fluctuation profiles for t10 and n10; OD; “E-block arm”.

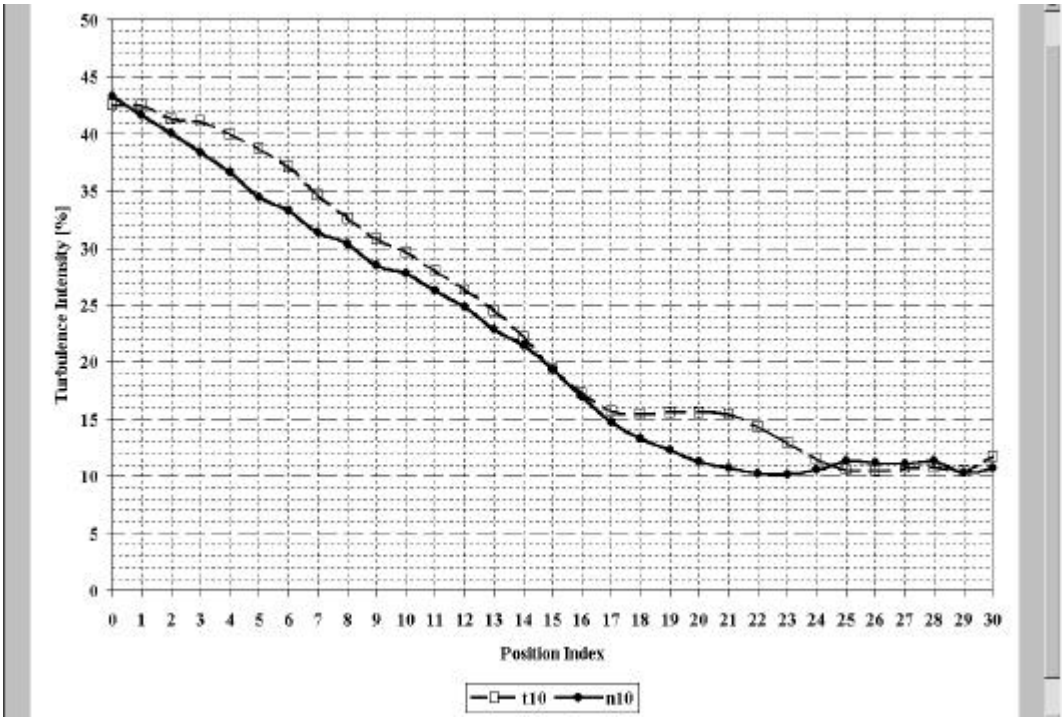

Figure 43: Turbulence intensity profiles for t10 and n10; OD; “E-block arm”.

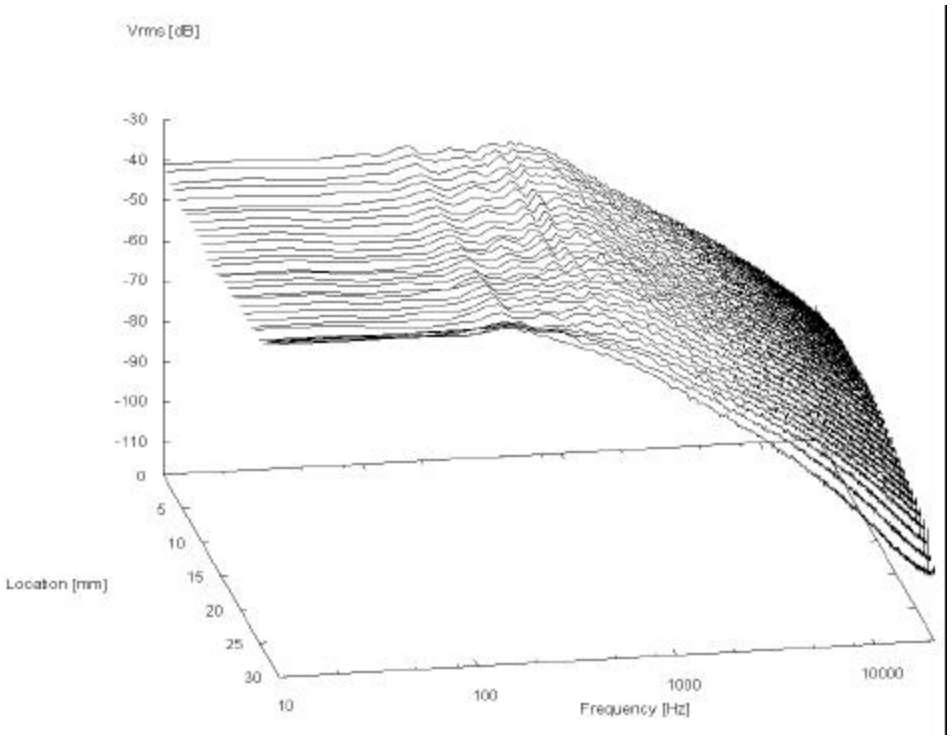


Figure 44: Power spectra of flow fluctuation; unobstructed flow; OD; “E-block arm”.

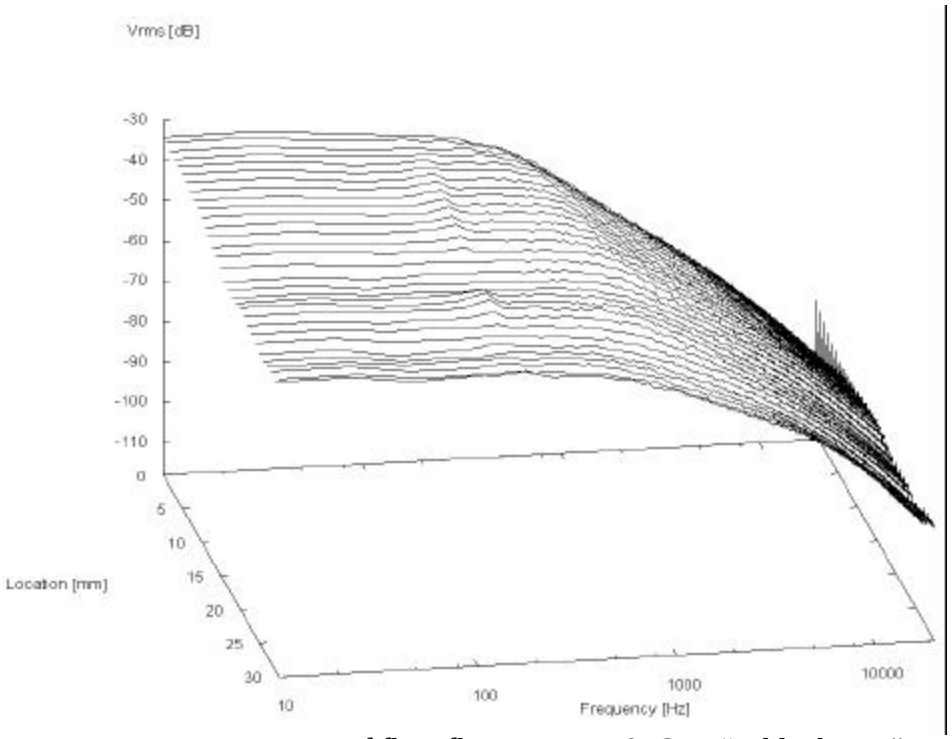


Figure 45: Power spectra of flow fluctuation; t10; OD; “E-block arm”.

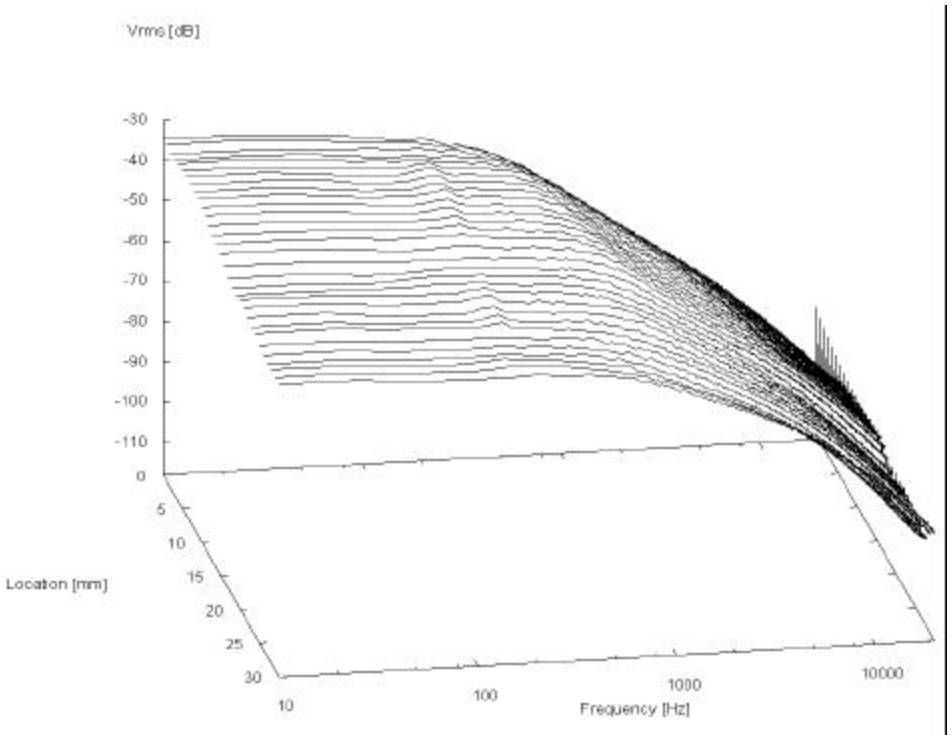


Figure 46: Power spectra of flow fluctuation; t12; OD; “E-block arm”.

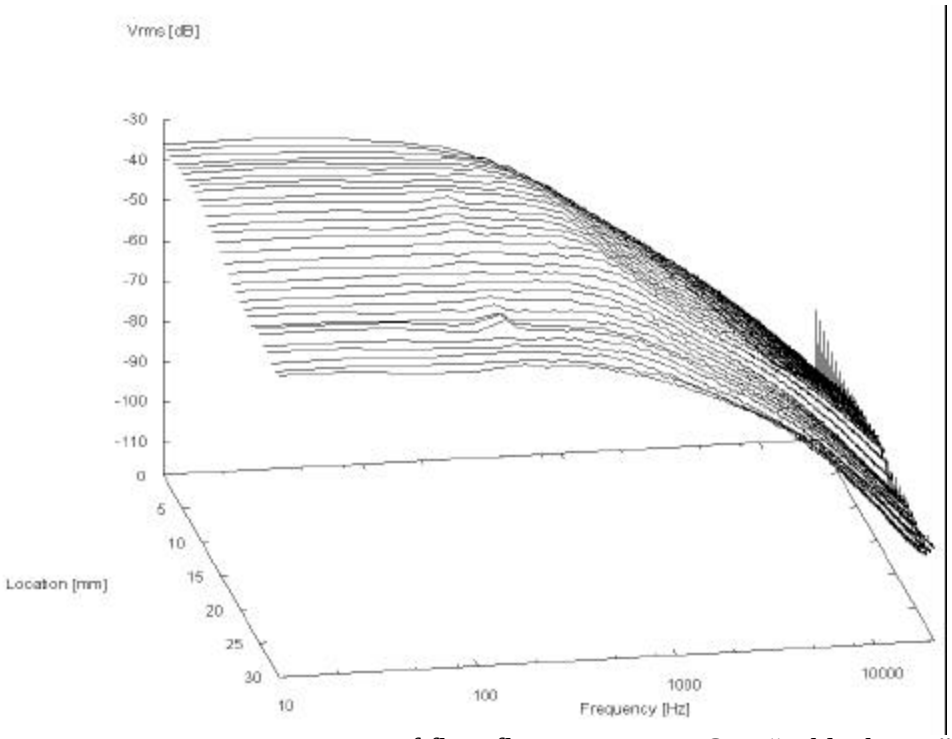


Figure 47: Power spectra of flow fluctuation; t14; OD; “E-block arm”.

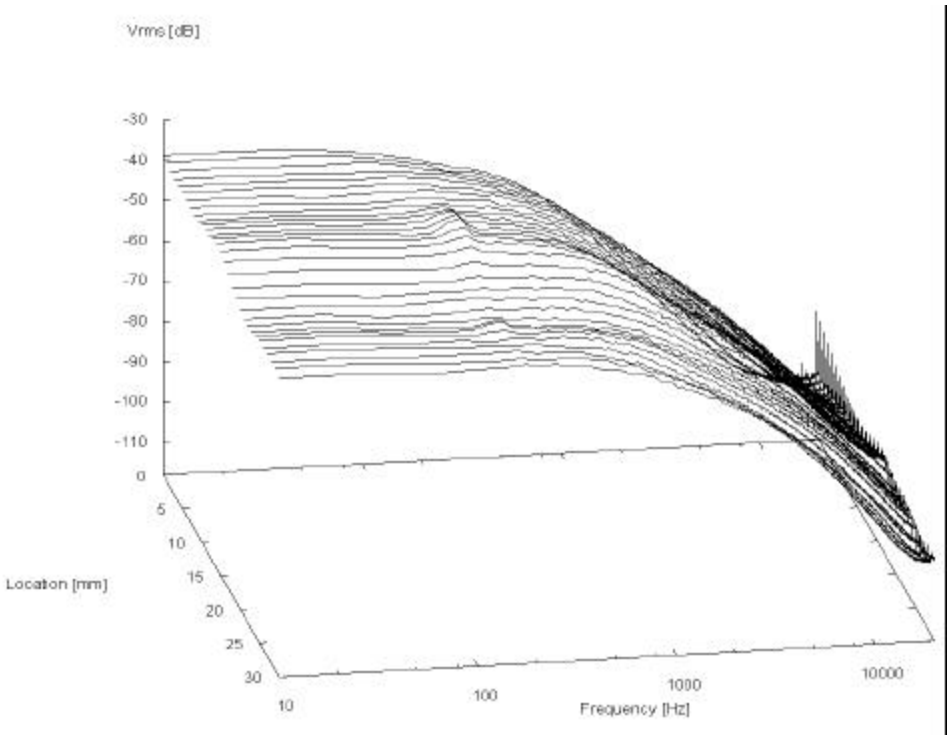


Figure 48: Power spectra of flow fluctuation; t16; OD; “E-block arm”.

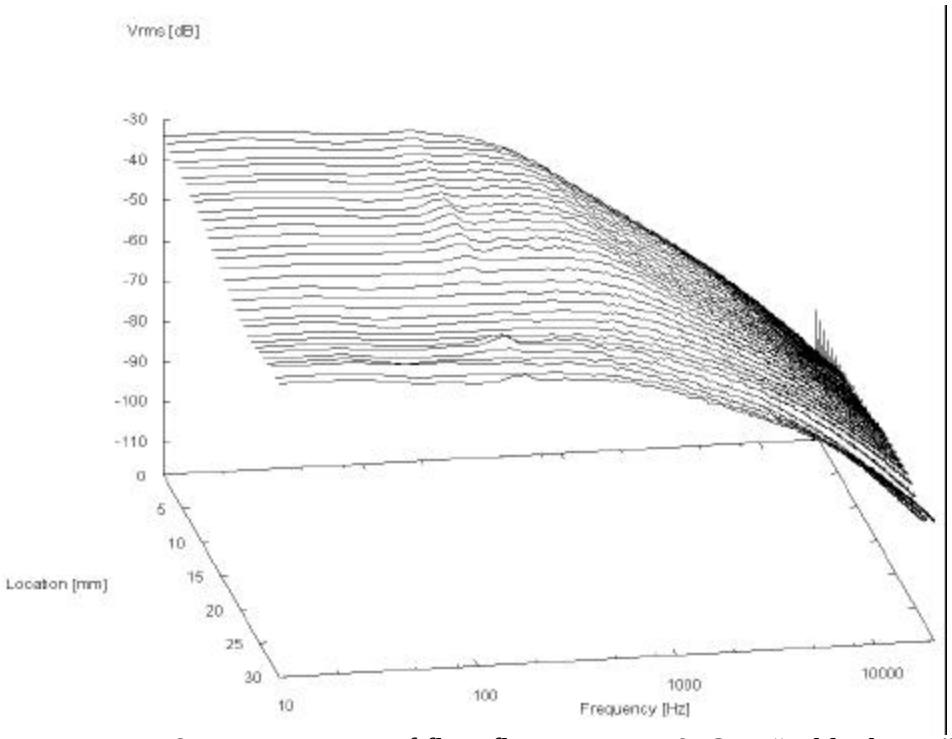


Figure 49: Power spectra of flow fluctuation; n10; OD; “E-block arm”.

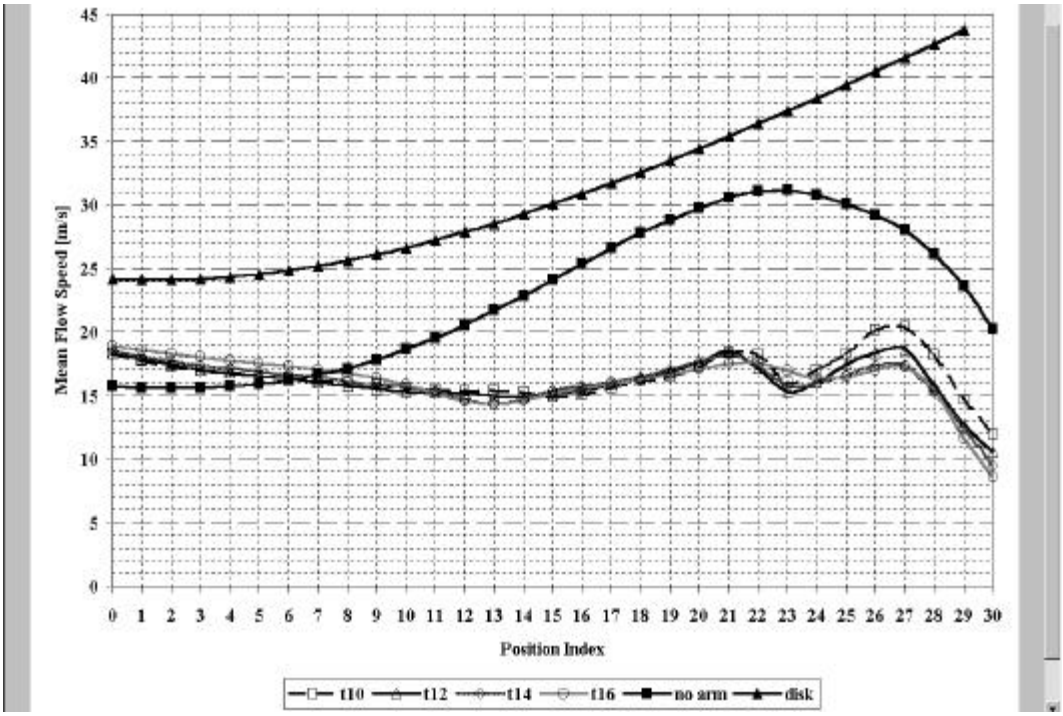


Figure 50: Mean flow speed profiles for unobstructed flow, t10, t12, t14, and t16; ID; “HSA”. Disk speed profile shown.

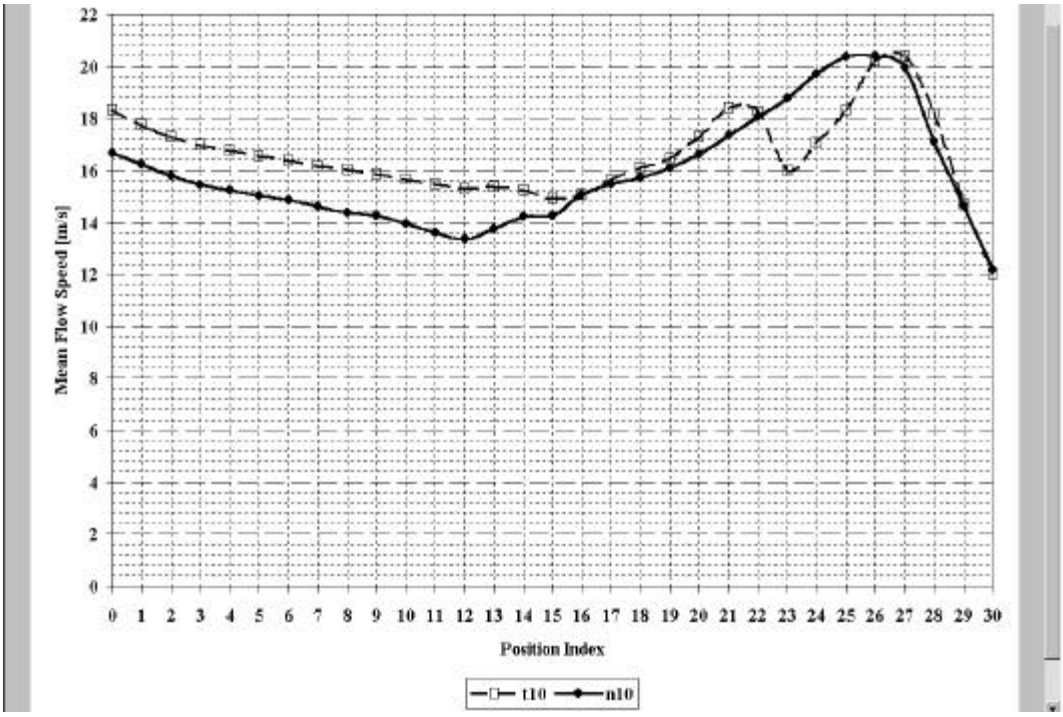


Figure 51: Mean flow speed profiles for t10 and n10; ID; “HSA”.

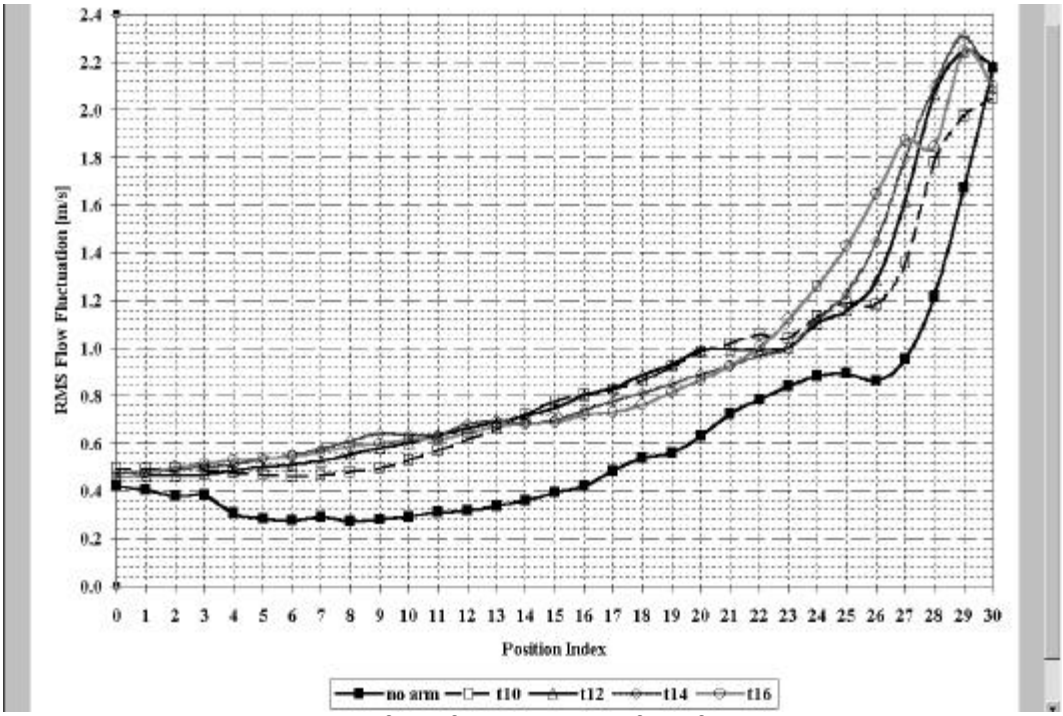


Figure 52: RMS flow fluctuation profiles for unobstructed flow, t10, t12, t14, and t16; ID; “HSA”.

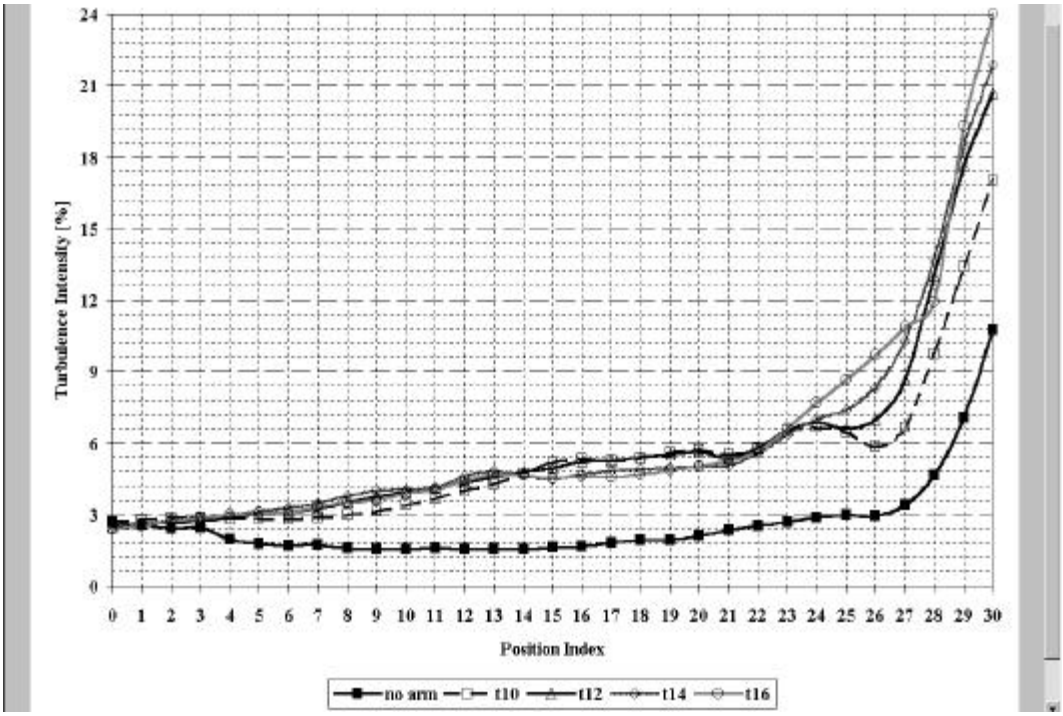


Figure 53: Turbulence intensity profiles for unobstructed flow, t10, t12, t14, and t16; ID; “HSA”.

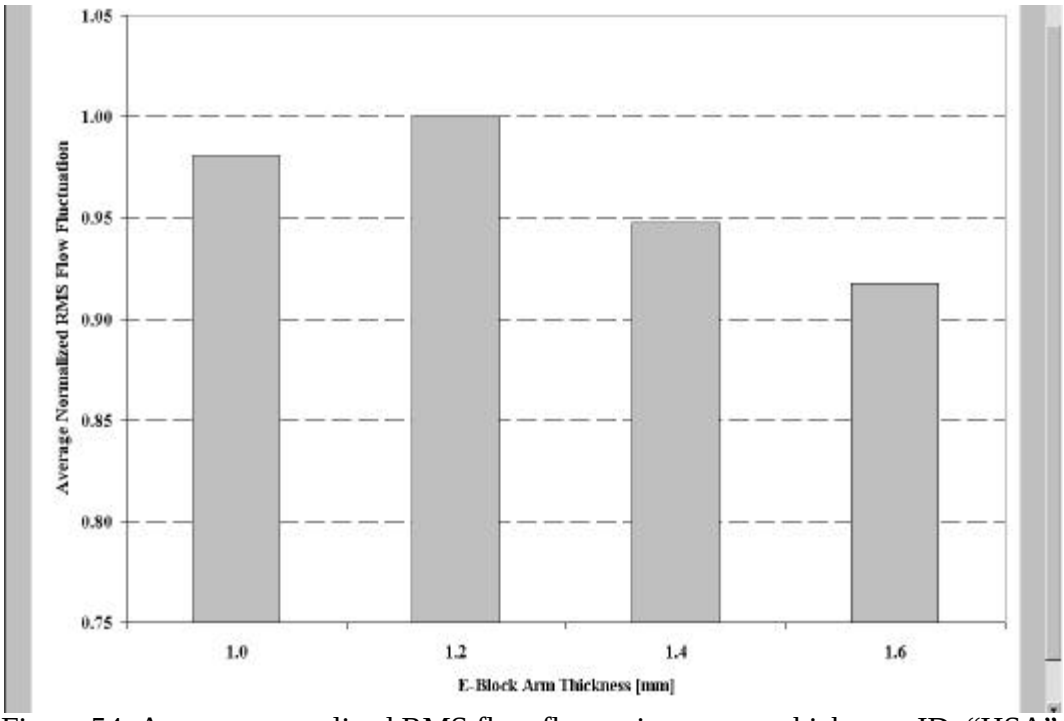

Figure 54: Average normalized RMS flow fluctuation vs. arm thickness; ID; “HSA”.

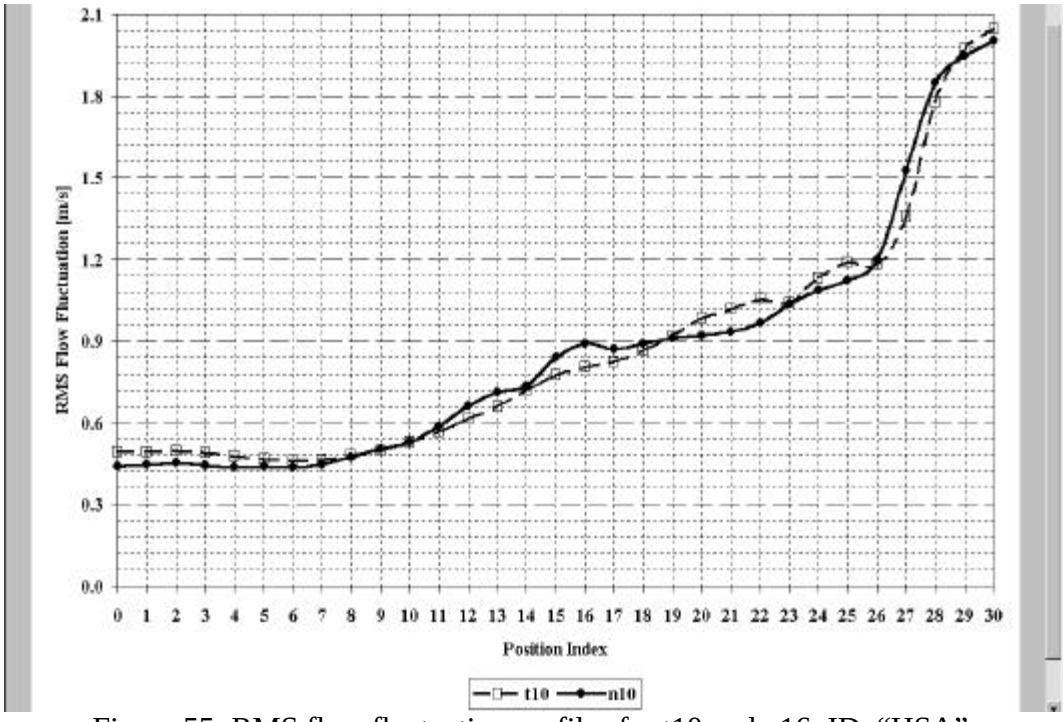

Figure 55: RMS flow fluctuation profiles for t10 and n16; ID; “HSA”.

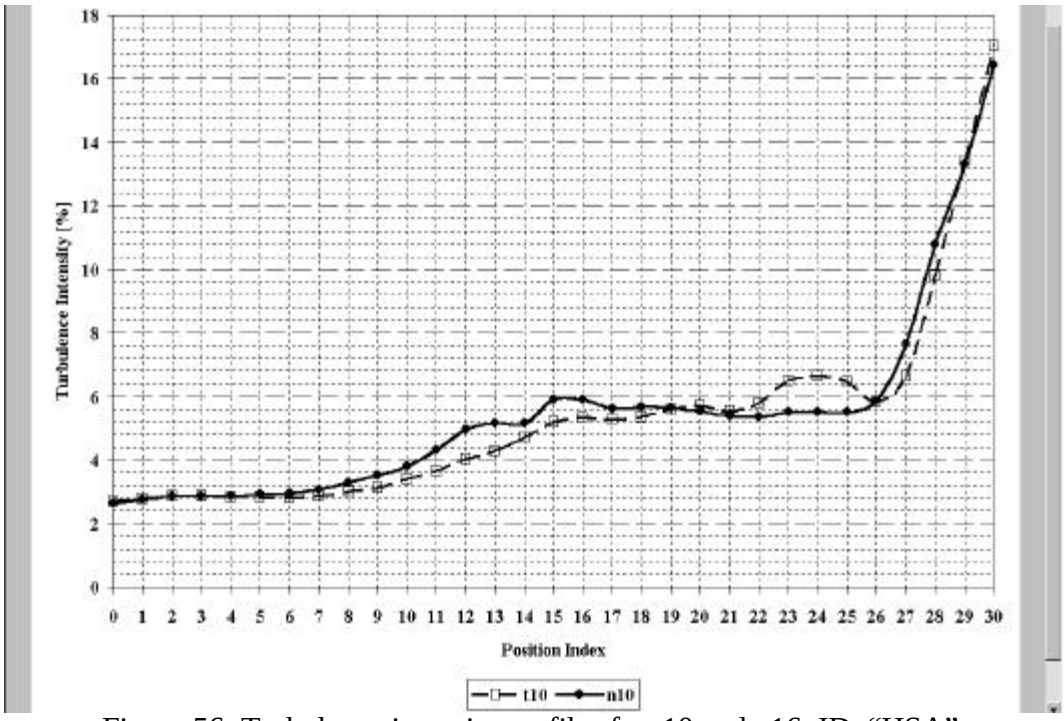

Figure 56: Turbulence intensity profiles for t10 and n16; ID; “HSA”.

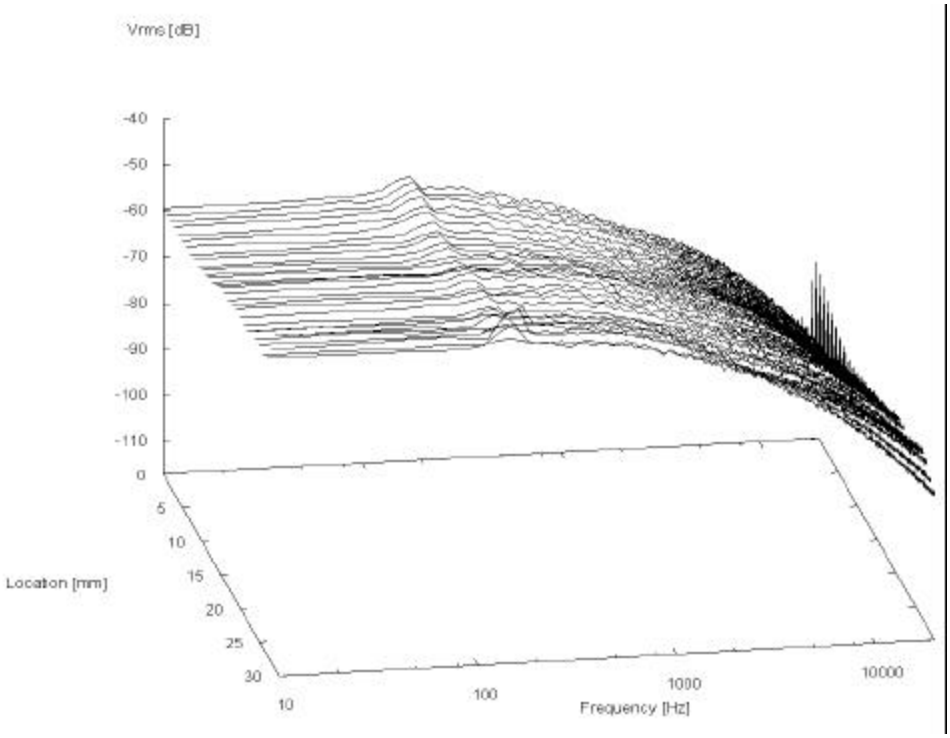

Figure 57: Power spectra of flow fluctuation; t10; ID; “HSA”.

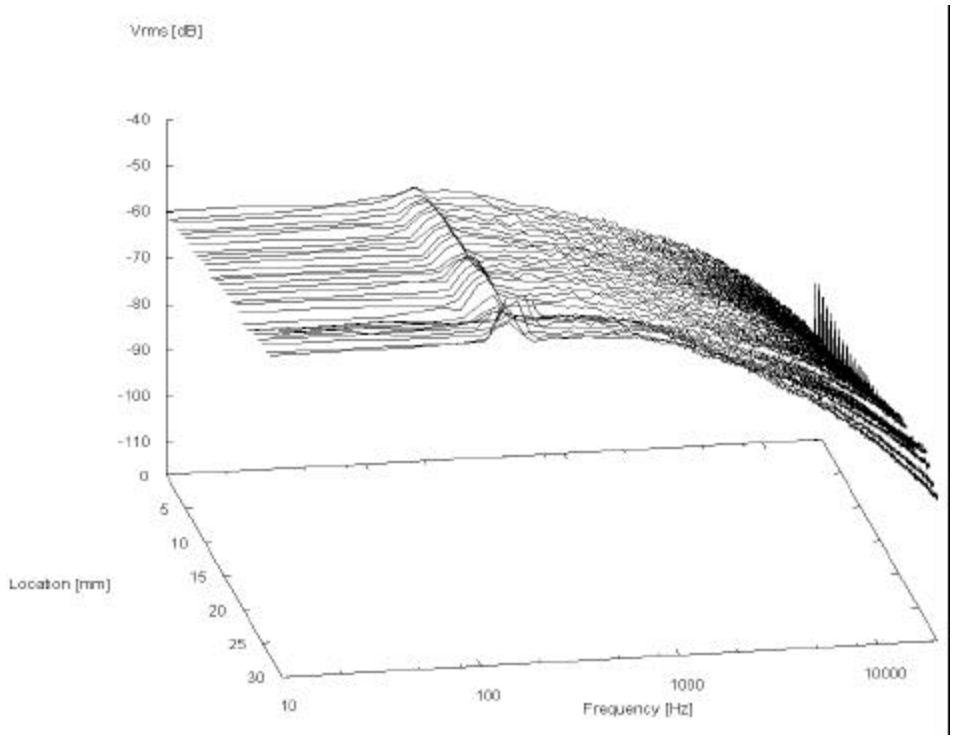


Figure 58: Power spectra of flow fluctuation; t12; ID; “HSA”.

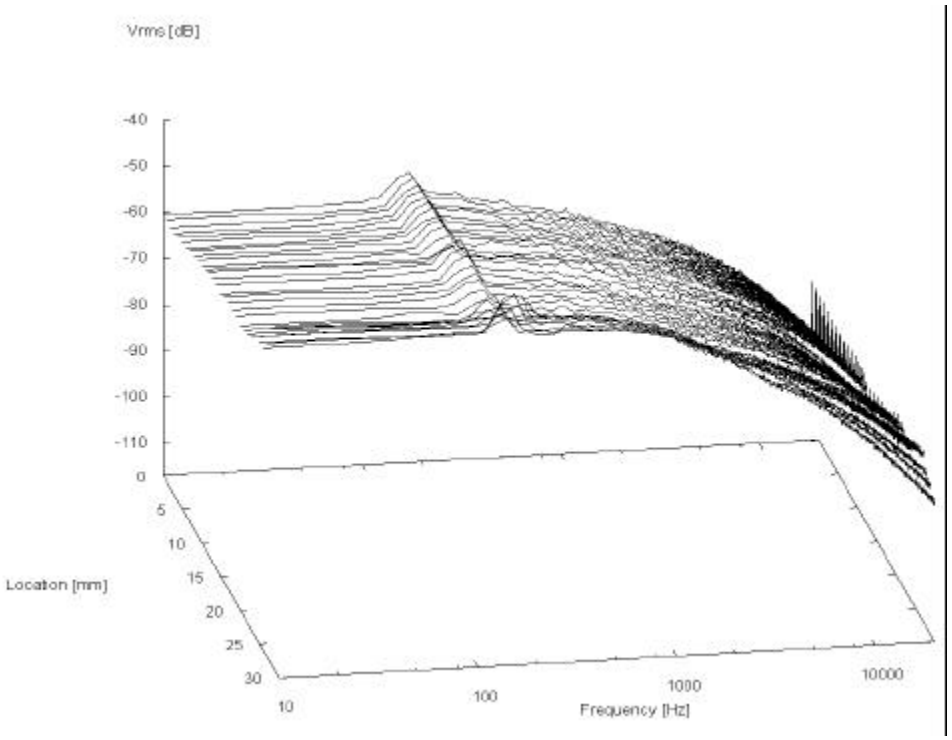


Figure 59: Power spectra of flow fluctuation; t14; ID; “HSA”.

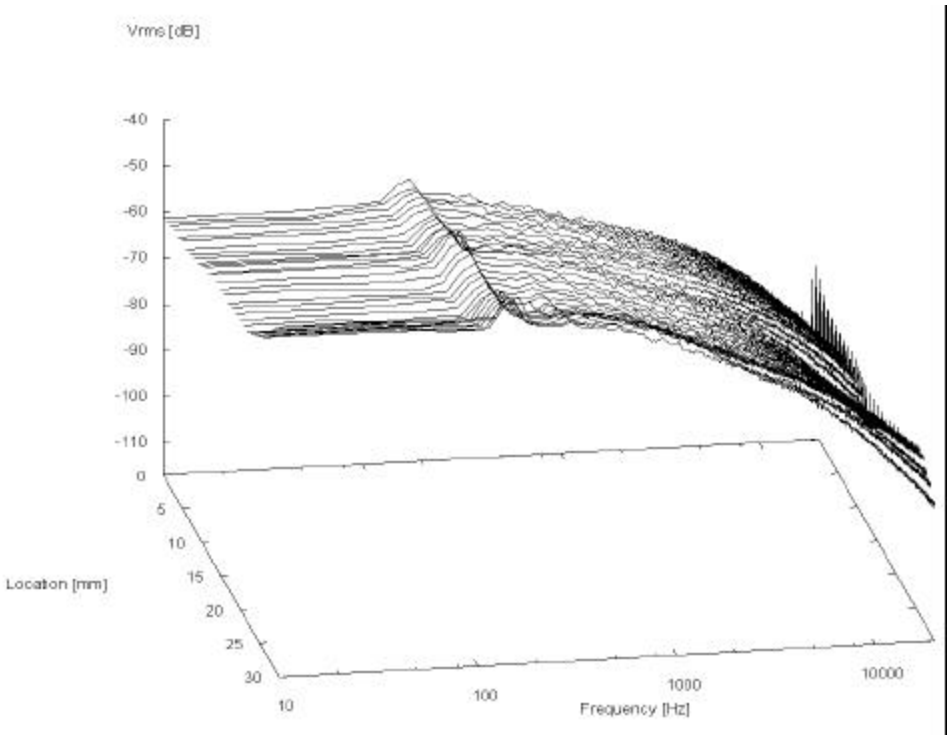


Figure 60: Power spectra of flow fluctuation; t16; ID; “HSA”.

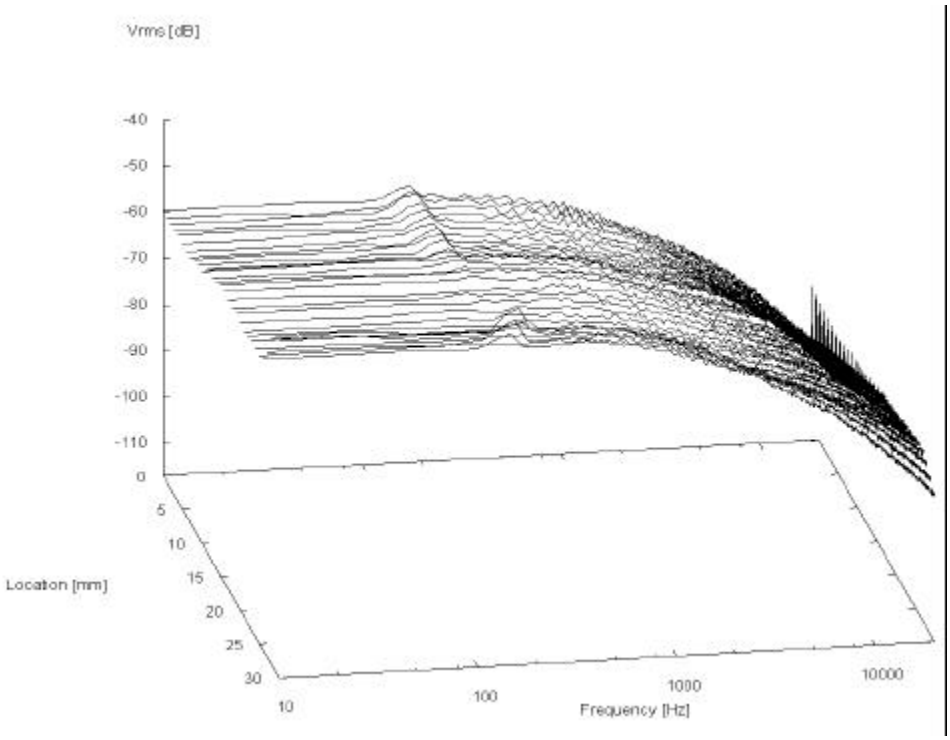


Figure 61: Power spectra of flow fluctuation; n10; ID; “HSA”.

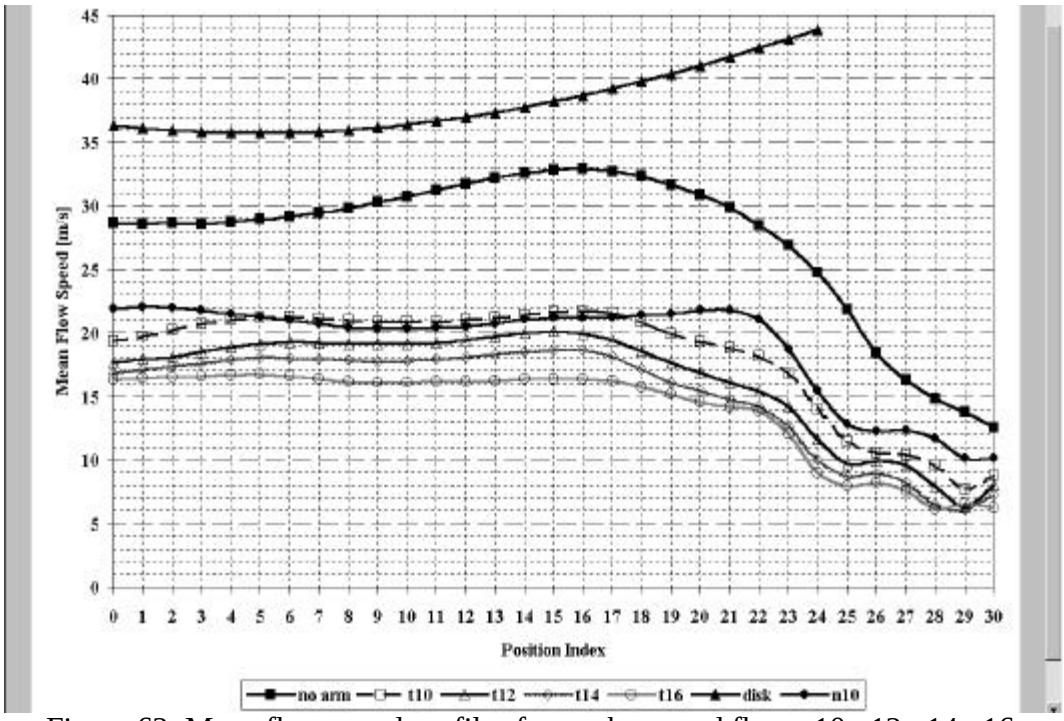


Figure 62: Mean flow speed profiles for unobstructed flow, t10, t12, t14, t16, and n10; MD; "HSA". Disk surface speed profile shown.

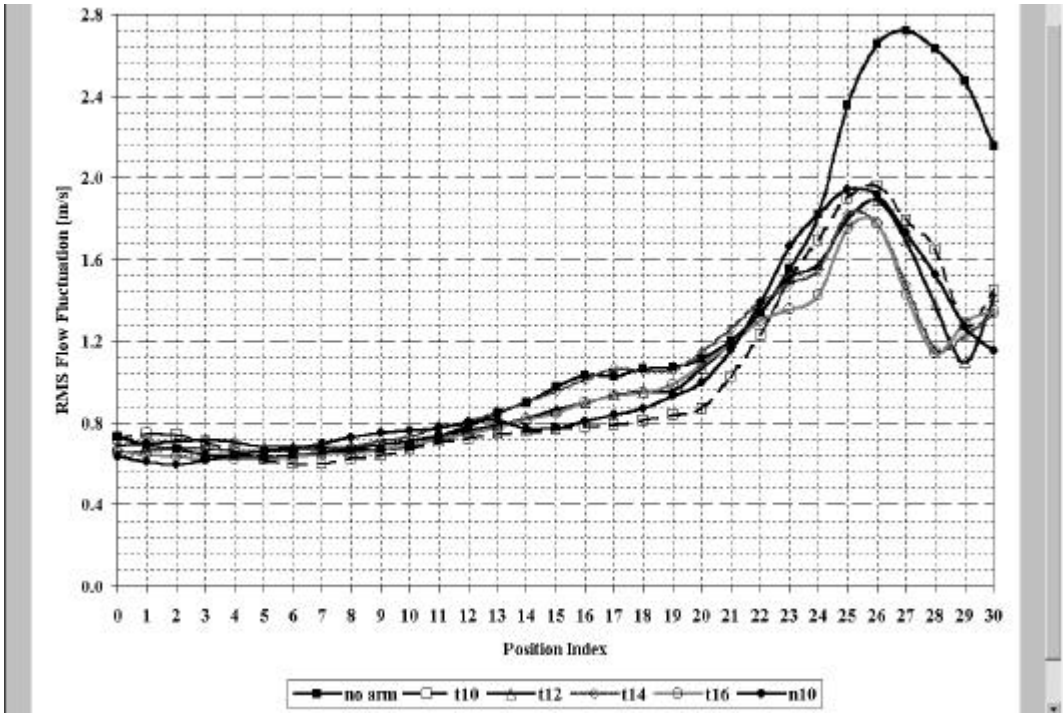


Figure 63: RMS flow fluctuation profiles for unobstructed flow, t10, t12, t14, t16, and n10; MD; "HSA".

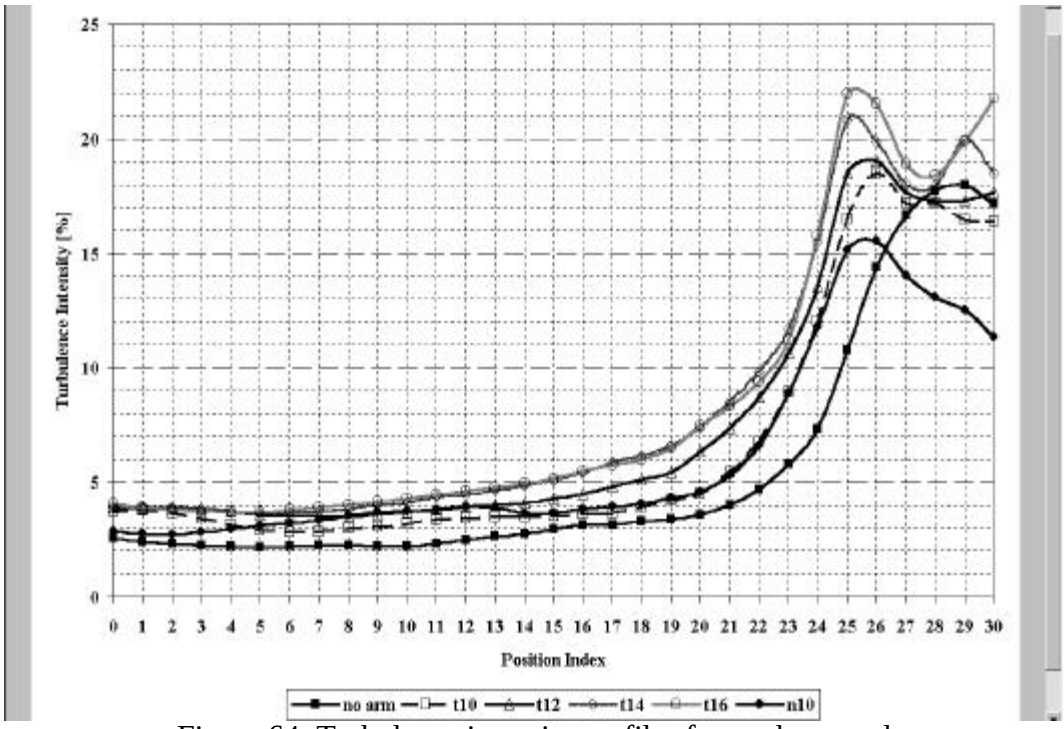


Figure 64: Turbulence intensity profiles for unobstructed flow, t10, t12, t14, t16, and n10; MD; “HSA”.

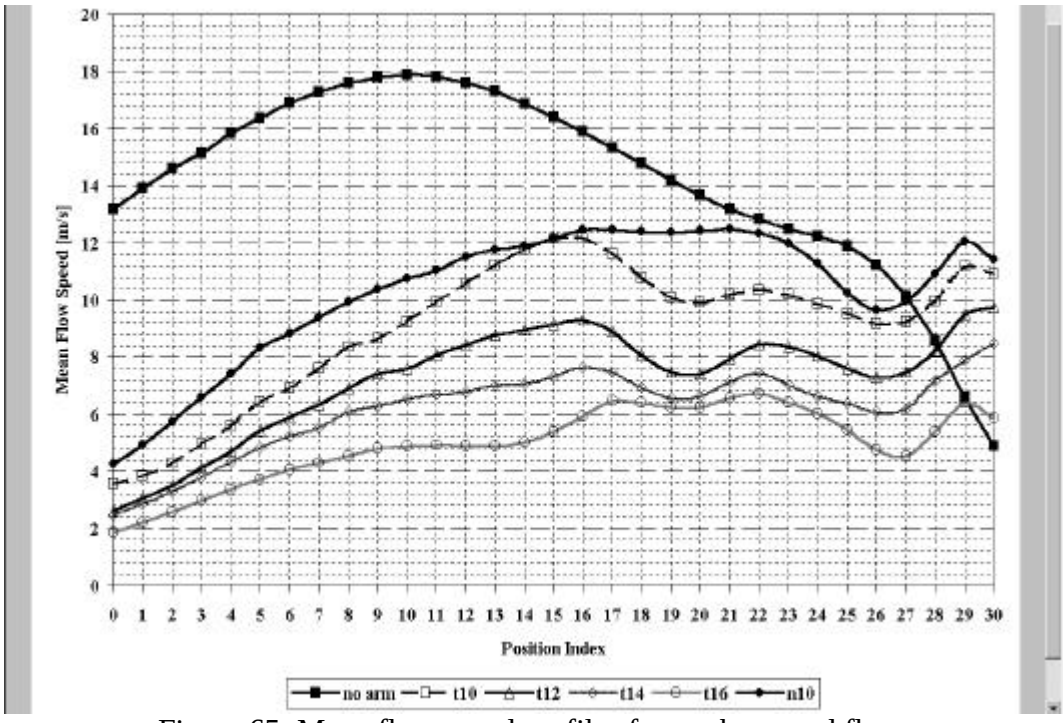


Figure 65: Mean flow speed profiles for unobstructed flow, t10, t12, t14, t16, and n10; OD; “HSA”.

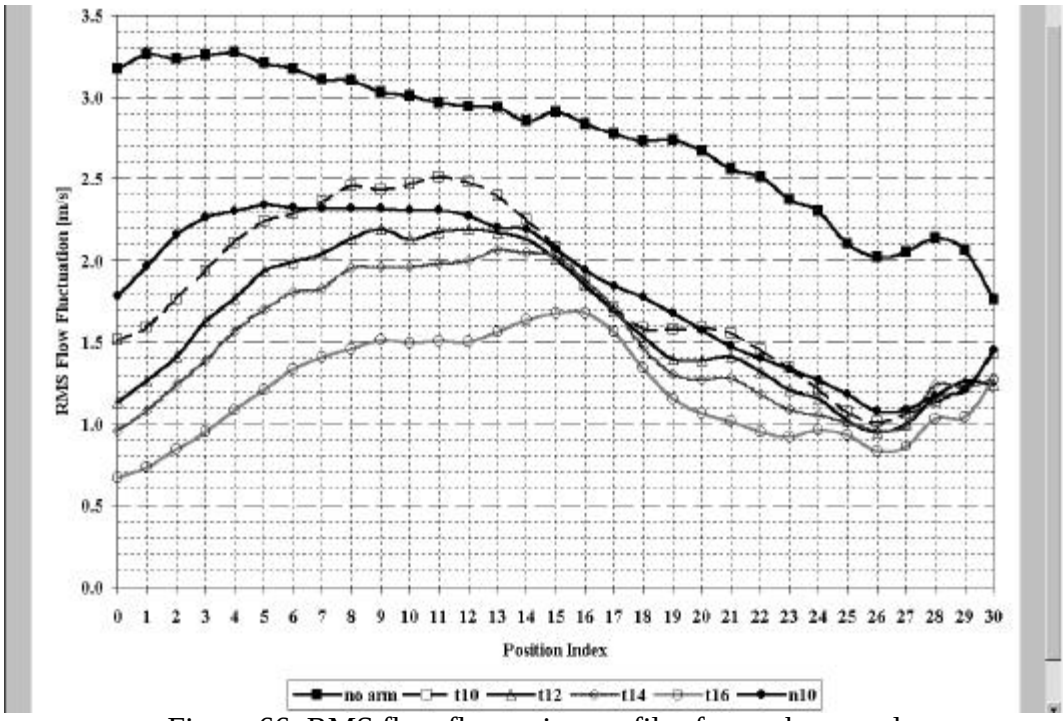


Figure 66: RMS flow fluctuation profiles for unobstructed flow, t10, t12, t14, t16, and n10; OD; “HSA”.

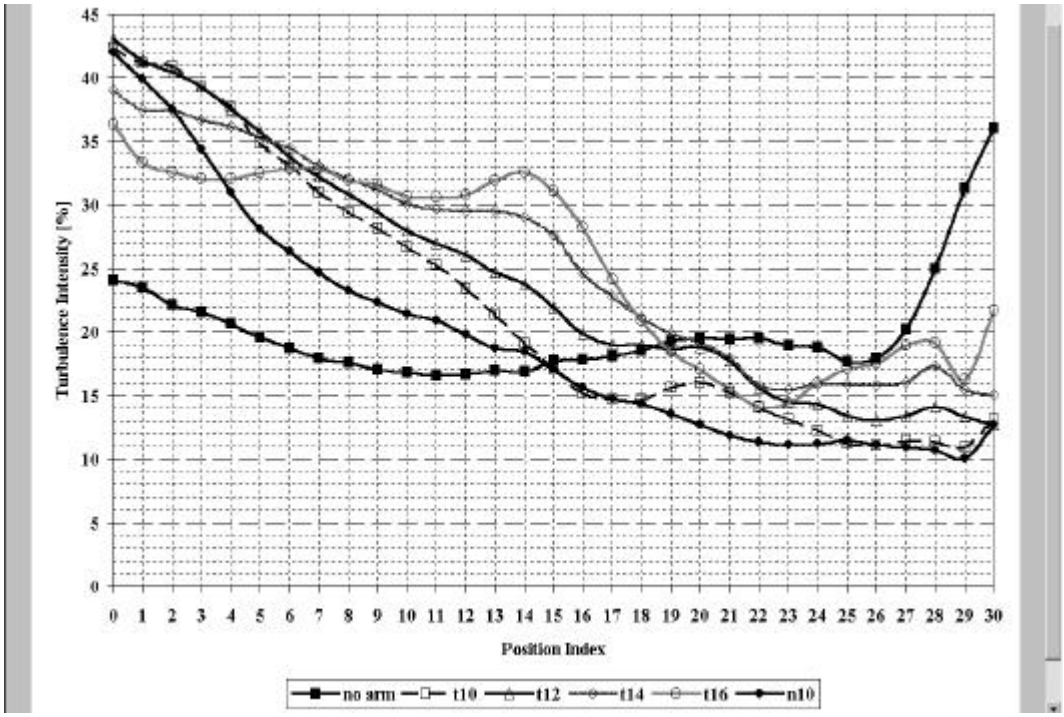


Figure 67: Turbulence intensity profiles for unobstructed flow, t10, t12, t14, t16, and n10; OD; “HSA”.